The Astrophysical Journal, 899:50 (19pp), 2020 August 10 https://doi.org/10.3847/1538-4357/ab9c1c

S62 and S4711: Indications of a Population of Faint Fast-moving Stars inside the S2 Orbit—S4711 on a 7.6 yr Orbit around Sgr A*

Florian Peißker[1], Andreas Eckart[1,2], Michal Zajaček[3,1], Basel Ali[1], and Marzieh Parsa[1]
[1] I.Physikalisches Institut der Universität zu Köln, Zülpicher Str. 77, D-50937 Köln, Germany; peissker@ph1.uni-koeln.de
[2] Max-Plank-Institut für Radioastronomie, Auf dem Hügel 69, D-53121 Bonn, Germany
[3] Center for Theoretical Physics, Al. Lotników 32/46, 02-668 Warsaw, Poland
Received 2020 May 18; revised 2020 June 9; accepted 2020 June 10; published 2020 August 11

Abstract

We present high-pass filtered NACO and SINFONI images of the newly discovered stars S4711–S4715 between 2004 and 2016. Our deep $H+K$-band (SINFONI) and K-band (NACO) data show the S-cluster star S4711 on a highly eccentric trajectory around Sgr A* with an orbital period of 7.6 yr and a periapse distance of 144 au to the supermassive black hole (SMBH). S4711 is hereby the star with the shortest orbital period and the smallest mean distance to the SMBH during its orbit to date. The used high-pass filtered images are based on coadded data sets to improve the signal to noise. The spectroscopic SINFONI data let us determine detailed stellar properties of S4711 like the mass and the rotational velocity. The faint S-cluster star candidates, S4712–S4715, can be observed in a projected distance to Sgr A* of at least temporarily $\leqslant$120 mas. From these stars, S4714 is the most prominent, with an orbital period of 12 yr and an eccentricity of 0.985. The stars S4712–S4715 show similar properties, with magnitudes and stellar masses comparable to those of S4711. The MCMC simulations determine confidently precise uncertainties for the orbital elements of S62 and S4711–S4715. The presence of S4711 in addition to S55, S62, and the also newly found star S4714 implies a population of faint stars that can be found at distances to Sgr A* that are comparable to the size of our solar system. These short orbital time period stars in the dense cluster around the SMBH in the center of our Galaxy are perfect candidates to observe gravitational effects such as the periapse shift.

Unified Astronomy Thesaurus concepts: B stars (128); Galactic center (565); Black holes (162); Relativistic stars (1392); Milky Way Galaxy (1054)

1. Introduction

Since the first detection of stellar proper motions around the supermassive black hole (SMBH) Sagittarius A* (Sgr A*) by Eckart & Genzel (1996) and Eckart & Genzel (1997), the number of detected S-stars increased with the development of larger telescopes and advanced analysis techniques (Ghez et al. 1998, 2002; Gillessen et al. 2009; Genzel et al. 2010; Gillessen et al. 2017; Gravity Collaboration et al. 2018a, 2020). Recently, we presented the orbit of S62 (Peißker et al. 2020a) as obtained with the Very Large Telescope (VLT, Chile). This star moves on a highly eccentric trajectory of $e = 0.976$ around Sgr A* with an orbital time period of $t_{\rm period} = 9.90 \pm 0.02$ yr. The distance of S62 to Sgr A* is $r_{\rm p} = 16.0$ au based on the well-defined orbital elements. The detection of this S-cluster member is in line with the observation of S55 (also known as S0-102, see Meyer et al. 2012). S55 has an orbital timescale of $t_{\rm period} = 12.8 \pm 0.1$ yr with an eccentricity of $e = 0.7209$ and has been detected with the KECKII telescope (Hawaii). The highly eccentric orbits of these faint stars (compared to $m_K = 14.1$ for S2) raise questions about their origin and uniqueness.

Stars in the central parsec of the Galactic Center, and in particular the S-cluster members, cannot have formed under classical conditions. Considering the presence of a high mass concentration and the resulting tidal forces excludes an in situ star formation scenario. This is also summarized in the phrase "Paradox of youth" formulated by Ghez et al. (2003). While Nayakshin et al. (2007) and Jalali et al. (2014) show how stars could have formed in the central parsec or even in the immediate vicinity of the SMBH, there remains the question of how stars can be placed on highly elliptical orbits with such small separations from Sgr A*. The Hills mechanism provides a matching theoretical background to describe the situation (Hills 1988). The Hills mechanism describes a three-body interaction including an SMBH and an eccentric stellar binary. When the binary (star-A and star-B) approaches SMBH, it gets disrupted and one companion (star-A) moves on a circularized orbit while the star-B gains the energy at the expanse of star-A and can be eventually expelled as a runaway star on an escaping hyperbolic orbit. This runaway star (star-B) could be kicked out of the binary system with hypervelocity (>300 km s^{-1}). Another possible product of this interaction could be two single stars on highly eccentric orbits, one with a smaller eccentricity and the other with a larger eccentricity (see numerical simulations done by several authors, Gould & Quillen 2003; Perets et al. 2007a; Löckmann et al. 2008; Bromley et al. 2012; Zajaček et al. 2014).

The three-body interaction including the massive black hole can effectively fill the "sparse region" around Sgr A*. In the classical quasi-spherical stellar cluster around Sgr A* with the power-law distribution of stellar number densities, there is a well-defined radius below which the number of stars statistically drops below one (Zajaček & Tursunov 2018),

$$r_1 = r_{\rm h} N_{\rm h}^{-\frac{1}{3-\gamma}}, \quad (1)$$

where $r_{\rm h}$ is the gravitational influence radius of Sgr A* ($r_{\rm h} \sim 2$ pc), $N_{\rm h}$ is the total number of stars inside $r_{\rm h}$, and γ is the slope of the stellar number density distribution, $n_\star \propto r^{-\gamma}$. For main-sequence stars, r_1 is expected to be at ~500 Schwarzschild radii (or about 40 au, Hopman & Alexander 2006). The Hills mechanism and scattering by massive perturbers (Perets et al. 2007a) can

effectively fill this "sparse region" with stars on orbits with large eccentricities and pericenter distances of $r_p \lesssim r_1$.

The S-stars S2, S55, and S62 are already three stars that orbit Sgr A* with orbital parameters that can be described with a high eccentricity and a small semimajor axis of a few milliparsecs. Hence, these stars could be dynamical remainders of the Hills mechanism. Two of them, namely S55 and S62, orbit Sgr A* with an orbital period of the order of 10 yr, which makes them convenient probes of general relativistic effects. This is especially encouraging as there might be even more stars with comparable orbital elements filling the "sparse region" around Sgr A*, as already predicted by Alexander & Morris (2003), where the authors introduce the existence of the so-called "squeezars." Alexander & Morris (2003) predict around 120 stars with $r_p < 120.0$ au and $t_{\rm period} < 60$ yr in the Galactic center.

In this work, we present the highly eccentric orbit of a new star inside the orbit of S2. We cover a full orbit of the new S-cluster member with the detection in the high-pass filtered NACO *K*-band images. The data reduction and the applied methods are described in Section 2. In Section 3, we show the results of the orbital fit and the simultaneous observation of S4711 in the SINFONI and NACO data. From the SINFONI data, we derive a Doppler-shifted line-of-sight (LOS) velocity. Additionally, we present Markov Chain Monte Carlo (MCMC) simulations of the orbital elements. From these simulations, we derive the uncertainties for the well-defined orbital elements of S4711 and S62. In Section 4, we discuss the results and conclude our analysis.

2. Data and Observations

In this section, we will briefly describe the analysis methods and the data-reduction steps. Most of the analysis steps are presented and based on Parsa et al. (2017), Peißker et al. (2020a), and Peißker et al. (2020b). It should be noted that the authors of Parsa et al. (2017) analyzed the orbit of the S-star S2 (also know as S0-2) and showed the relativistic Schwarzschild precession with this very NACO data set. This was later confirmed by Gravity Collaboration et al. (2020) and underlines the robustness of the data set.

2.1. Data Reduction

For this work, we used the SINFONI and NACO data sets that are already discussed, shown, and analyzed in (Peißker et al. 2019, 2020a, 2020b). For the *K*-band observations, we use the NAOS+CONICA (NACO) instrument with the adaptive optics (AO) guide star IRS7 located about 5.″5 north of Sgr A*. The *H*+*K* observations are carried out with the Spectrograph for Integral Field Observations in the Near Infrared (SINFONI). The optical guide star for the SINFONI AO correction is located 15.″54 north and 8.″85 east of Sgr A*. Both instruments were mounted at the Very Large Telescope (VLT) in Paranal/Chile and are now decommissioned. Standard data-reduction steps with the ESO pipeline were applied. For the SINFONI *H*+*K* data, we use DARK frames to correct for hot pixels. LINEARITY frames are taken to supervise the detector response. FLAT lamps measure the pixel-to-pixel response. DISTORTION frames are used to correct for optical distortions and to monitor the slitlet distances. Lastly, WAVE frames are taken in order to wavelength-calibrate the data. Since we also use NACO in the *K*-band imaging mode, the reduction steps are comparably short. We apply the FLAT field and bad pixel correction. For creating a mosaic, we shift the individual images in an 2048×2048 array to their related positions. Furthermore, the data from both instruments have been sky-corrected. The used data are listed in Appendix C.

2.2. Methods

For reducing the influence of overlapping point-spread function (PSF) wings, a low-pass filter is a suitable and efficient approach. We are subtracting a Gaussian flux density conserved smoothed image from the input image. For that, the size of the Gaussian filter should be close to the PSF size. In SINFONI, this is usually around 5–6 pixels corresponding to 62–75 mas and depends on the overall data quality. After the subtraction, we smooth the result again. In principle, the same Gaussian filter size is possible. However, we use different filter sizes of less than 6 pixel. The result that allows the best discrimination of densely packed stars from each other is then chosen manually. Since there is no loss in information, the process is stable against false positives (see also Peißker et al. 2020b).

Another method for analyzing the data is the high-pass filter, also known as the Lucy Richardson algorithm (Lucy 1974). Since noise can be associated with low frequencies, the high-pass filter helps to highlight image details that are above a self-defined threshold. It is known that the Galactic center and especially the S-cluster suffer from a spatially variable background. This leads, for example, to the creation of blended stars (Sabha et al. 2012). With this, a background subtraction is sufficient and needs to be adjusted for every data set because of different weather conditions and the varying number of high-quality observations. Cosmic rays, the influence of the detector cosmetics, readout errors, and the overall state of the data are noticeable error sources. The determination of the position of Sgr A* is based on the well-known and observed orbit of S2 (Parsa et al. 2017; Gravity Collaboration et al. 2019).

3. Results

Here, we present our results of the SINFONI and NACO data analysis. We show the orbit of S4711 and the detection of the star in the NACO and SINFONI data. From the latter, we extract a Doppler-shifted spectrum and derive an LOS velocity for S4711. Furthermore, we present the observation of S4712–S4715. Some of these S-stars are at least temporarily close to Sgr A*, with comparable properties to those of S4711. Complementary material can be found in the Appendix.

3.1. S4711 on a 7.6 yr Orbit around Sgr A*

The close passage of S2 did not allow sensitive observations of the region covered by the S4711 orbit in 2017 until 2019. However, for every year from 2004 to 2016, we can confirm several detections of S4711 in the high-pass filtered NACO *K*-band images (Figures 1 and 2). Source positions are derived via Gaussian fits to the objects in the images of each epoch. Since the positional determinations in the high-resolution images are not necessarily Gaussian-distributed, we used the median in the years between 2006 and 2010 to avoid outliers (Figure 3). Consider also the detailed description of the analysis given in Peißker et al. (2020a). Based on the positions derived from these data sets we were able to fit the orbit of S4711 (indicated by red data points in Figure 2). The resulting orbital elements are presented in Table 1.

The maximum distance of S4711 from Sgr A* is around 80 mas (≈6 pixel in the NACO images). Therefore, the star suffers blending and confusion with other objects in the

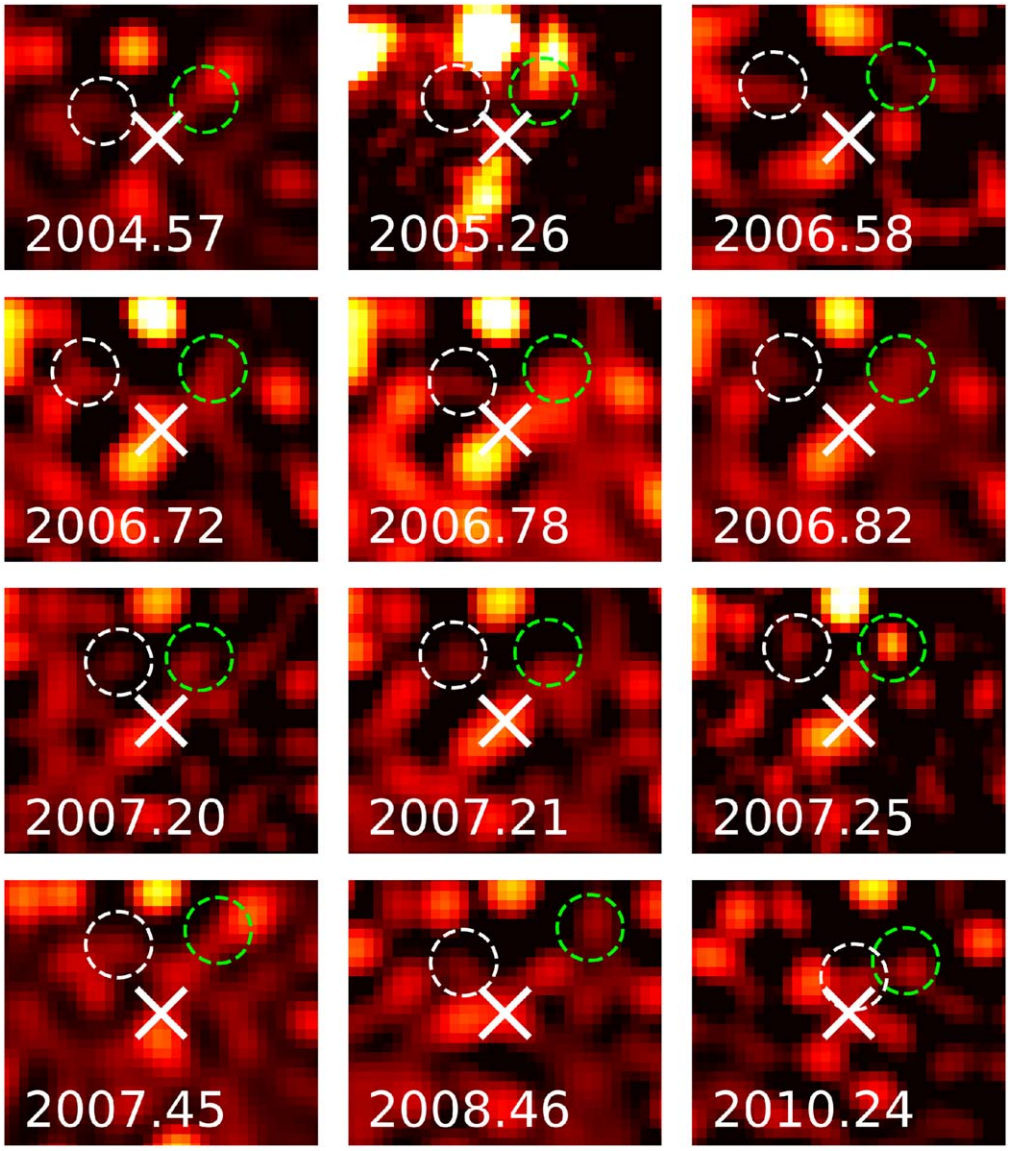

Figure 1. S4711 on its orbit around Sgr A*. Here, we present NACO *K*-band images that are high-pass filtered. Sgr A* is marked with a white cross and the position of S62 is marked with a green dashed circle. S4711 is highlighted by a white dashed circle. Orientation-wise, north is up and east is to the left. The size of every image in this figure is about $0\farcs44 \times 0\farcs37$.

crowded field. This effect is minimized because of the constant monitoring of the S-cluster in the last 25 yr but underlines the need for a sufficient number of high-quality observations.

Based on the NACO and SINFONI detection of S4711 (see Figures 1 and 4), we find a *K*-band magnitude of $m_K = 18.43 \pm 0.22$ with

$$m_{\mathrm{K,\ S4711}} = -m_{\mathrm{K,\ S2}} + 2.5 \times \log(\mathrm{ratio}), \tag{2}$$

with aperture photometry and a S2 *K*-band magnitude of 14.15 (Schödel et al. 2010). We use this method to derive the apparent magnitude m_K for all newly discovered stars (see Table 2). To determine the mass of these faint S-cluster stars (FSS), we adapt from Cai et al. (2018):

$$\lg\frac{M_{\mathrm{S}}}{M_{\odot}} = \mathrm{km}_K + b, \tag{3}$$

with $k = -0.192$ and $b = 3.885$. The authors of Cai et al. (2018) derive from a fit of the S-star properties presented in Habibi et al. (2017) the values for k and b. Using the same data from Habibi et al. (2017), we confirm $b = 3.885$ and use in the following $k = -0.1925$. Using Equation (3) with the values given in Habibi et al. (2017), we find an agreement with the stellar mass in the range of 5%–10% for the three discussed S-stars.[4] We adapt an error of $-1\,M_{\odot}$ and $+2\,M_{\odot}$. With that, Equation (3) provides an accessible approach for deriving the mass for the S-stars when no spectroscopic information is available. Consult Table 2 for the stellar mass of S62 and S4711–S4715.

In 2007, S4711 reaches it apoapse. Also, the distance between S4711 and S2 is sufficient enough to analyze the spectrum of the newly discovered star in the SINFONI data of the related year (Figure 5). We find an LOS velocity of $v_{\mathrm{Br}\gamma} = -291 \pm -55\,\mathrm{km\,s^{-1}}$. The depth of the HeI and Brγ[5]

[4] S1, S2, S4, S6, S7, S8, S9, and S12.

[5] Rest wavelength: HeI at 2.161 μm, Brγ at 2.166 μm.

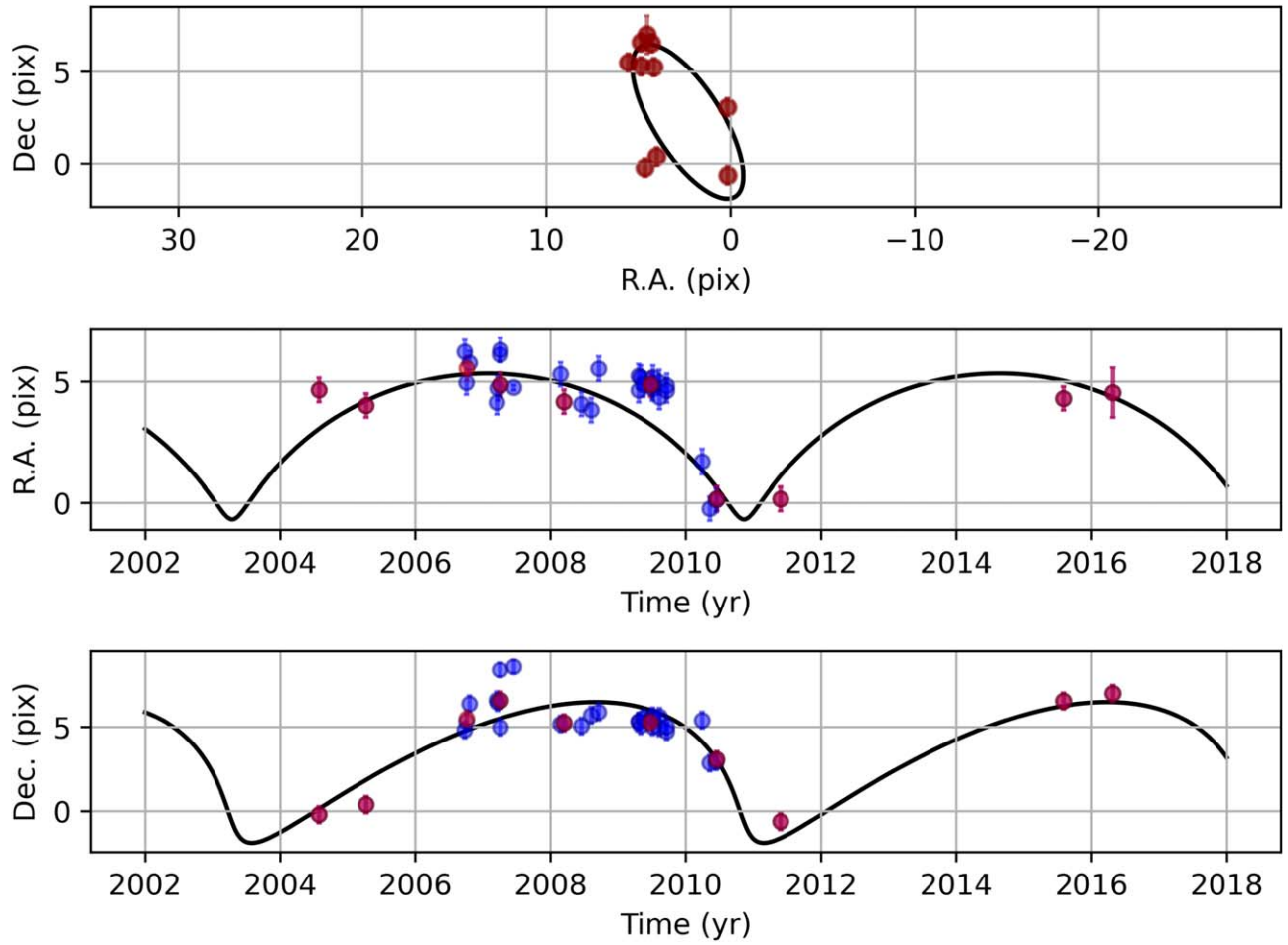

Figure 2. Orbit of S4711 where 1 pixel corresponds to 13.3 mas. The plot shows all available data points, with the typical uncertainties of ±6.5 mas based on the NACO data. Red data points represent the geometric median of most of the years except for 2004, 2005, 2011, 2015, and 2016. The blue data points show the data. Because of S17, S62 and the DSO/G2 object, an identification of S4711 between 2012 and 2013 is not possible without confusion. In 2014, NACO was not mounted at the VLT. In 2017 and 2018, the periapse passage of S2 hinders a successful observation of S4711.

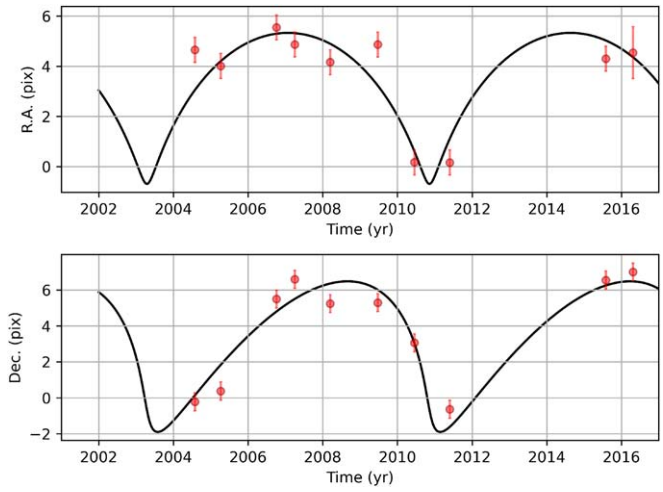

Figure 3. Median orbit of S4711. Here, we show the median of every year. The median is stable against the influence of outliers. 1 pixel corresponds to 13.3 mas. Similar to Figure 1, we set the units of the *y*-axis to [pixel] to underline the close distance to Sgr A*.

absorption features are comparable with the analysis of the S-cluster stars presented in Habibi et al. (2017). Because of the apoapse position of S4711, the derived LOS velocity is a lower limit of the range of possible Doppler-shifted values. The observed HeI line at 2.161 μm is actually a doublet, namely $7^3F - 4^3D$ at 2.16137 μm and $7^1F - 4^1D$ at 2.16229 μm (Lumsden et al. 2001). This "shoulder" is clearly detectable in the spectrum (Figure 5) and shows an asymmetrical shape. This points toward a low rotational velocity ($v \sin i$) of the star. A singlet would be the result of a high $v \sin i$ value. The presence of a rotational velocity, however, prolongs the lifetime of the star (Clark et al. 2018) and therefore possible in-spiral events that will be discussed in Section 4. Considering the critical study of the rotational velocity by Zorec et al. (2017), we determine for S4711 $v \sin i = 239.60 \pm 25.21\,\mathrm{km\,s^{-1}}$ with the FWHM of the 2.161 μm HeI line. Even though Slettebak et al. (1975) finds somewhat lower values for the Brγ line, the derived rotational velocity here is in a comparable range with the findings of Clark & Steele (2000) and Abt et al. (2002).

Furthermore, we derive from the shape of the Brγ line the spectral type of S4711. We use the NIR spectral atlas of Hanson et al. (1996) and follow the analysis presented in Eisenhauer et al. (2005) to determine the spectral type of S4711. For the Brγ line width (∼10 Å) and the spectrum, we find good agreement with the emission of a B8/9-V star with an effective temperature of about $T_{\mathrm{eff}} = 10{,}700$–$11{,}800$K (Tokunaga 2000).

Because of the maximum distance to Sgr A* of around 0.1 arcsec, the data selection is limited due to blending events

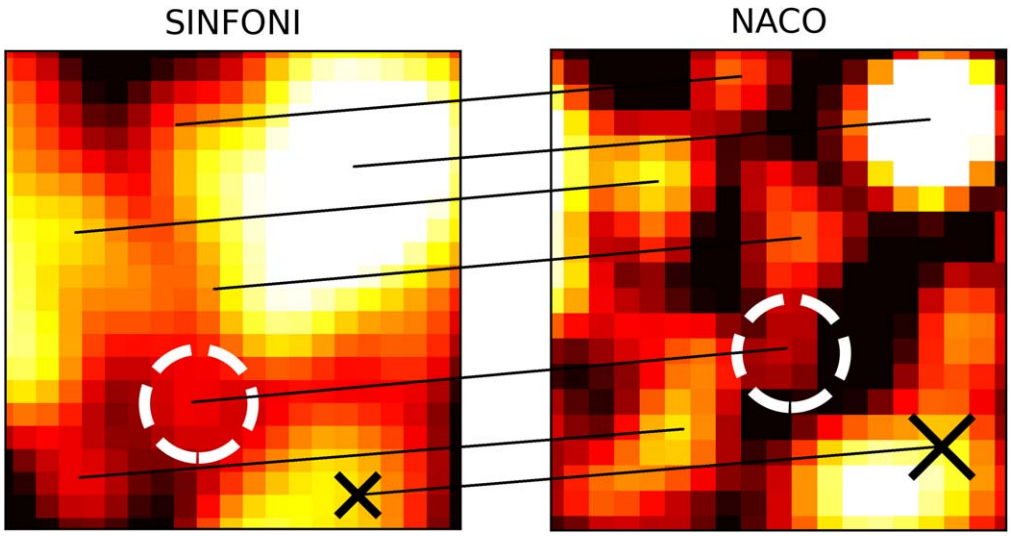

Figure 4. SINFONI and NACO detection of S4711 in 2007 based on high-pass filtered images. The S-star S2 is located in the upper right corner. Sgr A* is marked with a black cross. The white dashed circle indicates the position of S4711. The position of the stellar sources in the SINFONI and NACO data is consistent with each other. For comparison, we indicate the detection and position in both data sets with a black line. Based on the orbital fit, the chance of detecting S4711 is maximized because of its isolated position in 2007. We use 10,000 iterations to neglect the chance of a false positive. We use an artificial PSF with similar properties as a natural one. Because of the contrast and the subtracted background, some areas seem to be under-crowded compared to others. Since both instruments have a different plate scale, distances appear distorted. In every image, north is up and east is to the left.

Table 1
Orbital Parameters for S4711, S4712, S4713, S4714, S4715, and S62

Source	a (mpc)	e	i (°)	ω (°)	Ω (°)	$t_{\rm closest}$ (yr)	$t_{\rm period}$ (yr)
S62	3.588 ± 0.02	0.976 ± 0.01	72.76 ± 5.15	42.62 ± 2.29	122.61 ± 4.01	2003.33 ± 0.02	9.9 ± 0.3
S4711	3.002 ± 0.06	0.768 ± 0.030	114.71 ± 2.92	131.59 ± 3.09	20.10 ± 3.72	2010.85 ± 0.06	7.6 ± 0.3
S4712	18.038 ± 0.099	0.364 ± 0.032	117.28 ± 1.31	238.08 ± 3.43	166.38 ± 3.20	2007.12 ± 0.08	112.0 ± 2.9
S4713	8.016 ± 0.379	0.351 ± 0.059	111.07 ± 1.66	301.97 ± 8.02	195.06 ± 5.15	2000.03 ± 0.22	33.2 ± 2.5
S4714	4.079 ± 0.012	0.985 ± 0.011	127.70 ± 0.28	357.25 ± 0.80	129.28 ± 0.63	2017.29 ± 0.02	12.0 ± 0.3
S4715	5.756 ± 0.439	0.247 ± 0.040	129.80 ± 3.72	359.99 ± 5.38	282.15 ± 2.92	2008.05 ± 0.30	20.2 ± 2.4

Note. The 1σ uncertainty is based on the MCMC simulations. The orbital period was calculated assuming the Sgr A* mass of $(4.1 \pm 0.2) \times 10^6\,M_\odot$. The related uncertainty was determined by the error propagation.

and overlapping orbits of close-by stars (Figure 6). This explains the data point density that is presented in Figure 2. We conclude that the observation of S4711 is hindered by the brighter close-by S-stars. Especially close to the pericenter passage of S2 in 2018 (Gravity Collaboration et al. 2018b), a detection of S4711 is not possible. From the orbit plot of the closest S-cluster members presented in Figure 6, we find an angle between the orbit of S4711 and S62 of about 45°. In comparison with the periapsis distance of about 2 mas for S62, we find for S4711 the pericentre distance of

$$r_{\rm p} = a(1 - e) \simeq 0.7\ {\rm mpc}, \tag{4}$$

and using 0.04 pc ≈ 1000 mas, we get $r_{\rm p} \approx 12$ mas = 144 au. Considering the periapsis distance of 120 au for S2 as obtained by Gravity Collaboration et al. (2019), S4711 has a comparable pericenter distance to Sgr A*. Its apocenter distance is closer than that for S2 by ∼900 au; see Table 3. Hence, given that the periods of S4711 and S62 are shorter than 10 yr, these may serve as better probes for relativistic effects than S2.

3.2. Uncertainties of the Orbital Parameters

In Peißker et al. (2020a), we used a variation of the position of S62 with respect to Sgr A* by ±1 px to derive the uncertainties for the orbital elements. However, the orbit of S4711 is even shorter compared to S62. A variation of ±1 px overestimates the range of possible orbital solutions compared to the extent of the orbit of S4711. Hence, we use the Markov chain Monte Carlo (MCMC) affine-invariant ensemble sampler (Foreman-Mackey et al. 2013) with PYTHON to derive the uncertainties for S4711, S4712, S4713, S4714, and S4715. For

Table 2
Stellar Parameters for Known and Newly Discovered S-stars

Source	Magnitude ($\rm mag_K$)	Mass ($M_\odot$)
S62	16.1	6.1
S4711	18.4	2.2
S4712	18.4	2.2
S4713	18.5	2.1
S4714	17.7	2.0
S4715	17.8	2.8

Note. For the photometric results of S62 and S4711–S4715, we consistently use the S-cluster member S2 as a reference star. We use the Equation (3) to derive the mass of these S-cluster members. The mass of S62 is an updated value (see Peißker et al. 2020a). Typical uncertainties for the magnitude are ±0.2, and the stellar mass is in the range of $-1\,M_\odot$ and $+2\,M_\odot$ (Habibi et al. 2017; Cai et al. 2018; Peißker et al. 2020a).

Table 3
Additional Orbital and Relativistic Parameters for S62, S4711, S4712, S4713, S4714, S4715 Stars in Comparison with S2 Star

Star	r_p (au)	r_a (au)	v_p (km s^{-1}) (% of c)	Γ (10^{-4})	$z_{gr}c$ (km s^{-1})	$\delta\phi$ (arcmin)	$\dot{\Omega}_{LT}$ (arcsec yr^{-1})
S62	17.8 ± 7.4	1462.4 ± 11.0	20124 ± 4244 (6.7 ± 1.4)	46	685.5 ± 288.6	74.7 ± 31.0	5.1 ± 3.2
S4711	143.7 ± 18.8	1094.7 ± 28.7	6693 ± 494 (2.2 ± 0.2)	5.6	84.5 ± 11.8	10.3 ± 1.3	0.34 ± 0.07
S4712	2366 ± 120	5075 ± 122	1449 ± 54 (0.48 ± 0.02)	0.34	5.1 ± 0.4	0.81 ± 0.05	(5.1 ± 0.5) × 10^{-4}
S4713	1073 ± 110	2234 ± 144	2141 ± 153 (0.71 ± 0.05)	0.75	11.3 ± 1.3	1.8 ± 0.1	(5.8 ± 1.1) × 10^{-3}
S4714	12.6 ± 9.3	1670 ± 10	23928 ± 8840 (8 ± 3)	64	966.1 ± 713.5	104.6 ± 76.3	7.0 ± 7.6
S4715	894 ± 83	1480 ± 122	2253 ± 129 (0.75 ± 0.04)	0.90	13.6 ± 1.4	2.4 ± 0.2	(1.4 ± 0.4) × 10^{-2}
S2	119.3 ± 0.3	1949.9 ± 2.8	7582 ± 8 (2.527 ± 0.003)	6.8	101.7 ± 5.0	11.7 ± 0.6	0.19 ± 0.02

Note. From left to right, we list the star name, its pericenter distance (in au), its apocenter distance (in au), the pericenter velocity (in km s^{-1} and % of light speed), the relativistic parameter defined as $\Gamma = r_s/r_p$, the gravitational redshift $z_{gr}c$ (in km s^{-1}), the Schwarzschild precession $\delta\phi$ (in arcmin), and the Lense-Thirring precession rate of the ascending node $\dot{\Omega}_{LT}$ for the spin parameter of 0.5 (in arcsec per yer).

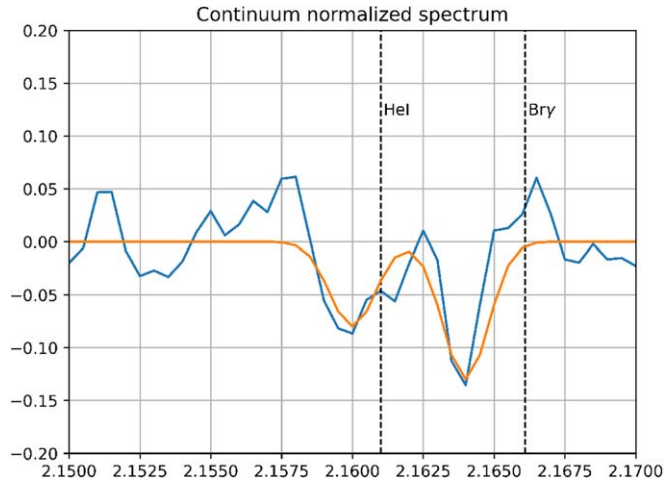

Figure 5. Normalized spectrum of S4711 extracted from the SINFONI data of 2007. We use an iris aperture with $r_{in} = 1$ px and $r_{out} = 3$ px and reference the selected aperture to Figure 4 (left plot). We find both a Doppler-shifted He*I* and Brγ absorption lines with a related LOS velocity of $v_{Br\gamma} = -291 \pm -55$ km s^{-1} (for comparable values see Habibi et al. 2017).

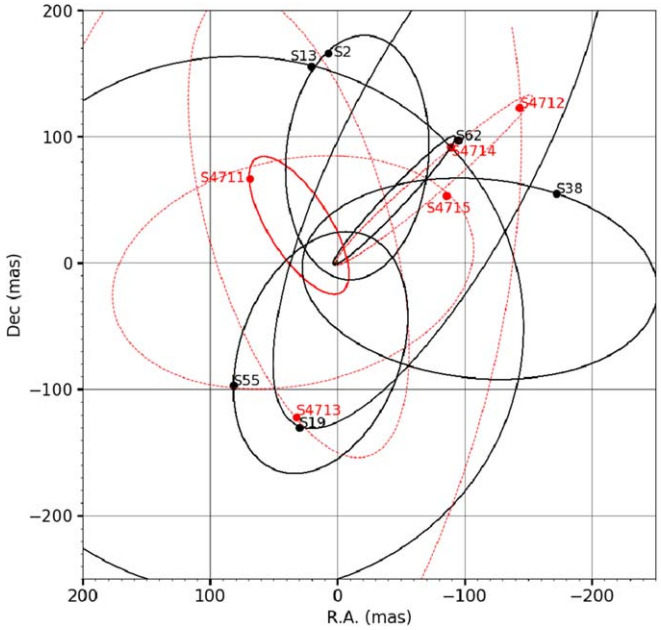

Figure 6. Orbits of several S-stars close to Sgr A*. The SMBH is located at the origin of the reference frame. The orbit of the reported S-cluster star S4711 is highlighted in solid red; the orbits of S4712, S4713, S4714 and S4715 are marked in dashed red. The dots represent the corresponding stellar position in 2007.

consistency, we also apply the MCMC-Metropolis-Hastings algorithm to the orbital elements of S62 (Figure 7). For the apriori distribution (prior), we use the results from the Keplerian fit model (Table 1). We then use iteration steps of 100 for the Bayesian updating. With this, we determine the mean of the posterior distribution of the Bayesian inference. For the mass and distance of Sgr A*, we adapt the values $4.15 \times 10^6\,M_\odot$ and 8.3 kpc from Parsa et al. (2017); Gillessen et al. (2017), and Gravity Collaboration et al. (2019). The 1σ uncertainties (68% confidence interval) for the S-stars investigated here are all in a comparable range (see Table 1). If the range of the uncertainties for an orbital parameter is not symmetrically distributed, we use the maximum value of the interval. We find that the MCMC sampler shows a satisfying compact probability for most parameters where the mean is almost identical with the prior (Figure 8). A broader posterior distribution would result in large uncertainties for the orbital parameters.

3.3. Expected General Relativistic Effects

To determine which of the newly identified faint S-stars are good probes of post-Newtonian effects, we first determine the relativistic parameter following Parsa et al. (2017):

$$\Gamma = \frac{r_s}{r_p}, \tag{5}$$

where r_s is the Schwarzschild radius of Sgr A*, $r_s = 1.21 \times 10^{12}(M_\bullet/4.1 \times 10^6\,M_\odot)$ cm, and $r_p = a(1-e)$ is the pericenter distance of the star. We list the values of Γ in Table 3. We see that S4714 and S62 have the largest values of Γ, followed by S4711, which has a Γ comparable to S2. Since the period of S4711 is less than half of the S2 period, its monitoring can reveal post-Newtonian effects twice as fast. The remaining stars, S4712, S4713, and S4715, have a Γ an order of magnitude smaller than S4711, hence they are weaker relativistic probes.

Following our analysis in Peißker et al. (2020a), we calculate the Schwarzschild periapsis shift (see Weinberg 1972) for S62, S4711–S4715 stars using

$$\delta\phi = \frac{6\pi G}{c^2}\,\frac{M}{a(1-e^2)} = \frac{3\pi}{1+e}\Gamma. \tag{6}$$

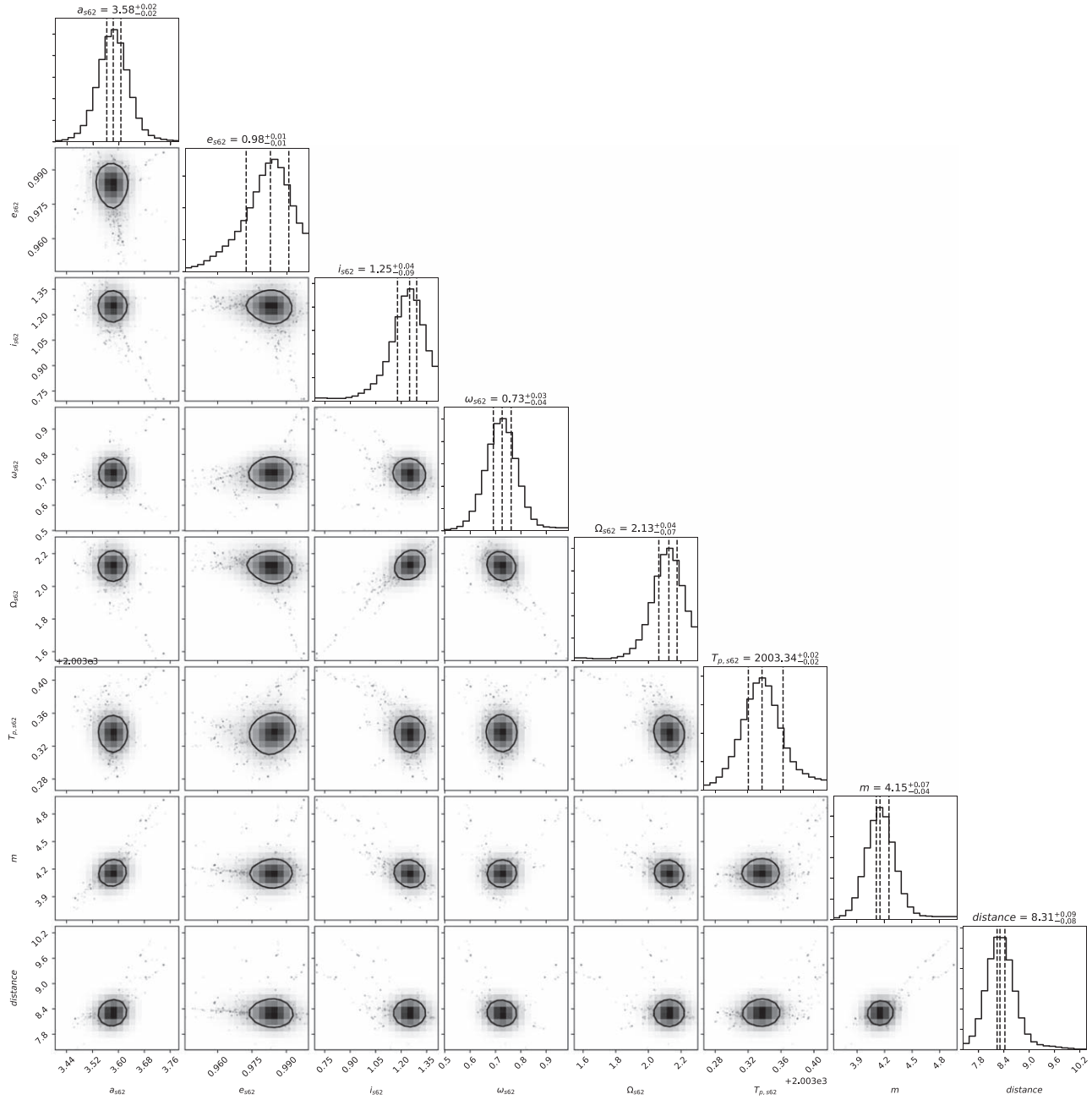

Figure 7. MCMC simulations for the six orbital elements based on a Keplerian model for S62. Additionally, two more parameters describing the mass and distance of Sgr A* are shown. The 1σ uncertainty shows compact shapes throughout the simulations. The presented quantiles correspond to the median (0.5) and the 1σ central interval (0.16, 0.84).

In Table 3, we list the values for all the stars. The largest reliable shift per period is for S62, $\delta\phi = 74.7 \pm 31.0$ arcmin,[6] and for S4714 $\delta\phi = 104.6 \pm 76.3$ arcmin, albeit with a large uncertainty. S4711 has a comparable Schwarzschild precession, $\delta\phi = 10.3 \pm 1.3$ arcmin, to the S-cluster star S2, $\delta\phi = 11.7 \pm 0.6$ arcmin.

Since the first detection of the two stars in 2002 (S62) and 2004 (S4711), several periapse passages have been performed. Because of the periapse shift of S4711, a detectable orbit shift could be observed in the next 10–20 yr. In addition, the orbital trajectory of S62 should be shifted by almost 5° between 2023 and 2033. Since the bright star S2 is passing by the Sgr A* region every 15 yr, the observation of the periapse passages of S62 and S4711 may be challenging, in particular since one needs to measure orbital sections before and after their passage.

For the remaining faint stars, S4712, S4713, and S4715, we obtained an order of magnitude smaller shifts per period, $\delta\phi = 0.81 \pm 0.05$, 1.8 ± 0.1, and 2.4 ± 0.2 arcmin, respectively, which follows from their values of Γ or in other words, from larger pericenter distances due to smaller eccentricities and larger semimajor axes. Another general relativistic parameter, which affects the observed wavelength of spectral lines, is the gravitational redshift, which can be

[6] The value of 9.°9 in Peißker et al. (2020a) is a misprint.

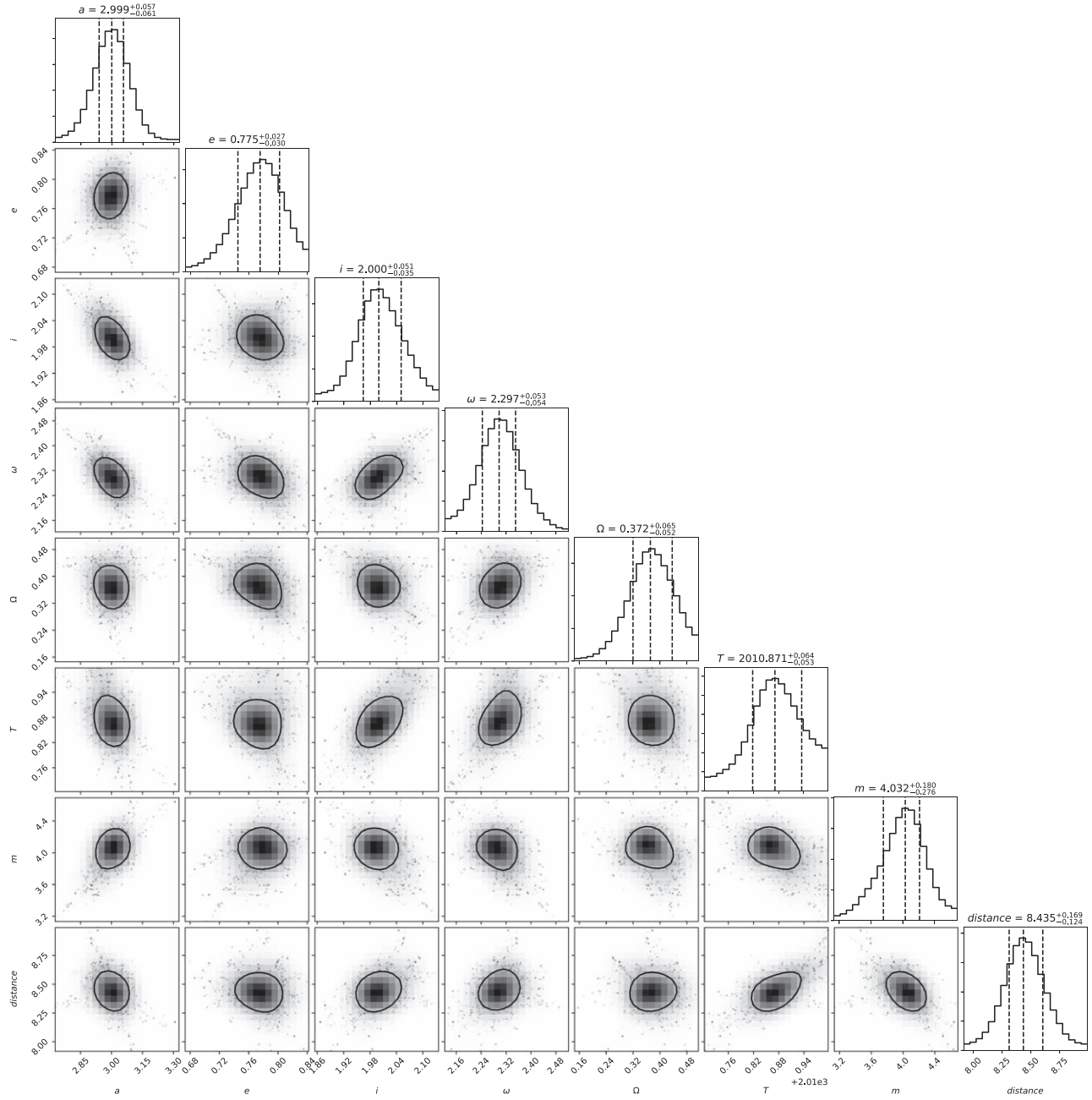

Figure 8. MCMC simulations for the six orbital elements based on a Keplerian model for S4711. As mentioned in the text, the mean distribution shows a satisfying agreement with the prior. In addition to the six orbital elements, we also show the MCMC posterior distribution for the mass and distance of Sgr A*.

expressed as

$$z_{\rm gr}c = c\left[\left(1 - \frac{r_{\rm s}}{r}\right)^{-1/2} - 1\right] \lesssim \frac{c\Gamma}{2}, \tag{7}$$

where the upper limit on the right is the approximate value at the pericenter (the approximation applies for $\Gamma \ll 1$). In Figure 9, in the left panel, we show the total radial velocity of the stars, including the radial Doppler shift and the gravitational redshift. In the right panel, we depict the gravitational redshift alone, which is the largest at the pericenter for each star. The values of the gravitational redshift for all the stars are listed in Table 3. The largest gravitational redshift in the S-cluster so far appears to be for S4714 with $z_{\rm gr}c = 966.1 \pm 713.5\,{\rm km\,s^{-1}}$, followed by S62 with $z_{\rm gr}c = 685.5 \pm 288.6\,{\rm km\,s^{-1}}$. The gravitational redshift of S4711 $z_{\rm gr}c = 84.5 \pm 11.8\,{\rm km\,s^{-1}}$ is within the uncertainty comparable to the value for S2. The remaining faint stars have a gravitational redshift of the order of $10\,{\rm km\,s^{-1}}$.

In addition, for S-stars with pericenter distances of the order of 1000 $r_{\rm s}$ and less, it is of great interest to measure the Lense-Thirring (LT) precession of the ascending node, since this would provide an independent probe of the black hole spin (Waisberg et al. 2018). For a star on an elliptical orbit around the SMBH, the LT precession of Ω can be calculated as follows (Merritt 2013a)

$$\dot{\Omega}_{\rm LT} = \frac{2G^2M^2\chi}{c^3a^3(1-e^2)^{3/2}} = \Gamma^2\frac{\chi c}{2r_{\rm a}}\sqrt{\frac{1-e}{1+e}}, \tag{8}$$

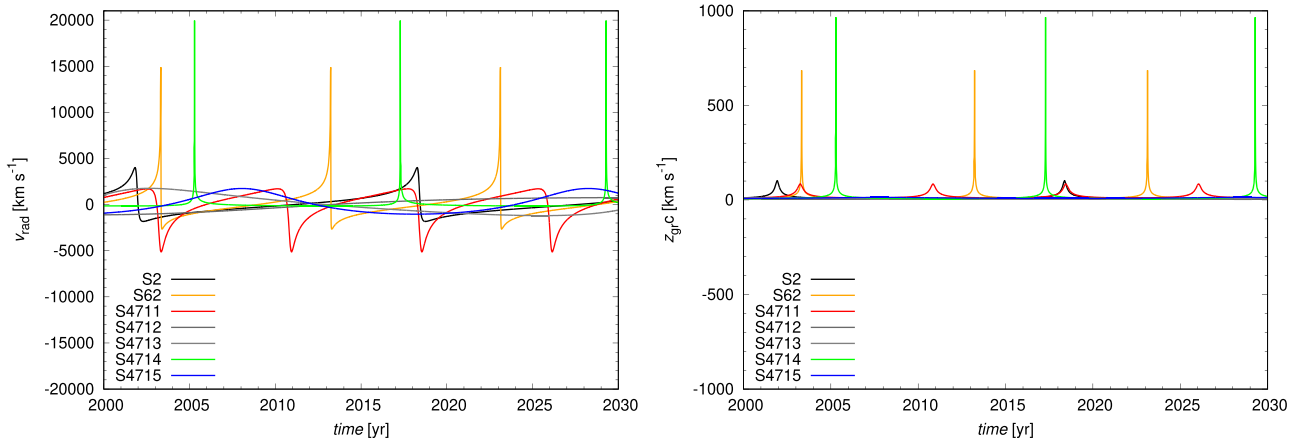

Figure 9. Total radial velocity (left panel) and the gravitational redshift (right panel) expressed in km s^{-1} as a function of time (in years) calculated based on the orbital elements in Table 1 for all the faint stars (S62, S4711, S4712, S4713, S4714, and S4715). S2 is also depicted for comparison.

where χ is the dimensionless spin of the black hole ($0 < \chi < 1$). We list the values of $\dot{\Omega}_{\rm LT}$ in arcseconds per year for all the sources in Table 3 for the assumed spin of $\chi = 0.5$, which was chosen based on the spin constraints inferred from modeling the total and polarized flux density of NIR flares ($\chi \geqslant 0.4$, Meyer et al. 2006). The rate of the LT precession is generally larger than that for the S2 star; in particular we obtained the largest mean value for S4714, $\dot{\Omega}_{\rm LT} = 7.0 \pm 7.6$ arcsec yr^{-1}, followed by S62 with 5.1 ± 3.2 arcsec yr^{-1}. S4711 has the larger rate of the LT precession, $\dot{\Omega}_{\rm LT} = 0.34 \pm 0.07$ arcsec yr^{-1} than the S2 star, which is expected to have $\dot{\Omega}_{\rm LT} = 0.19 \pm 0.02$ arcsec yr^{-1}. The remaining faint S-stars, namely S4712, S4713, and S4715, have values of $\dot{\Omega}_{\rm LT}$ at least one order of magnitude smaller.

However, even for S62 and S4714, which have the best prospects for the Lense-Thirring precession, the monitoring will have to last for at least 20 yr to reliably measure the spin. The criterion of Waisberg et al. (2018), $f_{\rm w} = a(1-e^2)^{3/4}$, is $f_{\rm w} \sim 954\, r_{\rm s}$ for the star S62 and $f_{\rm w} \sim 765\, r_{\rm s}$ for S4714. Following Waisberg et al. (2018), it would be necessary to monitor S4714 26 yr using 120 total observations with 10 μ *as* astrometric precision to detect the spin of $\chi = 0.9$. For S62, the campaign would have to last ∼41 yr for the same parameters.

3.4. Spatial Orbital Velocity

According to the Ramanujan approximation of an ellipse (see e.g., Almkvist & Berndt 1988), the orbital distance U of S4711 traveled during its 7.6 yr orbit can be calculated via

$$U_{\rm S4711} \approx (a+b)\pi\left(1 + \frac{3\lambda^2}{10 + \sqrt{4-3\lambda^2}}\right) \quad (9)$$

with $\lambda = \frac{a-b}{a+b}$ where a is taken from Table 1. The semiminor axis b can be calculated using the eccentricity e and the semimajor axis a with

$$b = \sqrt{a^2 - e^2}. \quad (10)$$

For S4711, we derive a value of $U_{\rm S4711} \approx 18.29$ mpc for the orbital length. In combination with its orbital time period, we derive a mean space velocity for S4711 to around 1540 km s^{-1} which equals about 0.5%c. For S62, we derive with the values given in Table 1 a orbital distance of $U_{\rm S62} \approx 22.11$ mpc with a mean 3d velocity of about 1370 km s^{-1} = 0.3%c. Applying this analysis to S2 with the orbital elements from Gravity Collaboration et al. (2018a) and Gravity Collaboration et al. (2019), we get $U_{\rm S2} \approx 31.42$ mpc and a mean 3D velocity of 1915.46 km s^{-1} = 0.4%c.

3.5. Indication for a Reservoir of Faint Stars Close to Sgr A*

The analysis of the NACO and SINFONI data reveals not only the existence of S4711, but also shows that there are several FSS candidates (Figure 10). The results of the observation of these FSS candidates are summarized in the following. For clarity, we follow the nomenclature introduced here and call them S4712, S4713, S4714, and S4715 to underline their uniqueness.

S4712: this S-cluster member can be observed between 2008 and 2015. Because of S2, S19, and S13, a detection before 2008 and after 2015 is not free of confusion. The orbital elements are based on the Keplerian fit of the NACO data and are listed in Table 1.

S4713: compared to S4712, the observation of S4713 is limited to the years 2006 to 2010. Like for S4712, the stars S2, S19, S55, and S175 hinders a confusion-free observation of S4713 before and after 2006 and 2010.

S4714: the faint star S4714 can be observed for 4 consecutive years. In contrast to S4712 and S4713, the orbital time period is much smaller and is determined to be around 12 yr (see Table 1). The orbital time period is in line with S55 and S62. These two S-stars are also hindering the observation of S4714 because of blending effects.

S4715: S4715 has a longer orbital period than S2 star, which is 20.2 ± 2.4 yr. Together with S4712 and S4713, these are longer-period newly discovered faint S stars in comparison with S62, S4711, and S4714. Because of the crowded S-cluster, it should be noted that we do not observe a full orbit of S4712, S4713, S4714, and S4715. Because of the observation in several consecutive years, a blend star scenario (Sabha et al. 2012; Peißker et al. 2020a) can be excluded.

S4716: as shown in Figure 10, we find another S-cluster member between S19 and S38 that we name S4716 to underline the character of the source. However, we observe this object in the NACO data set of 2008 and 2009. Because of

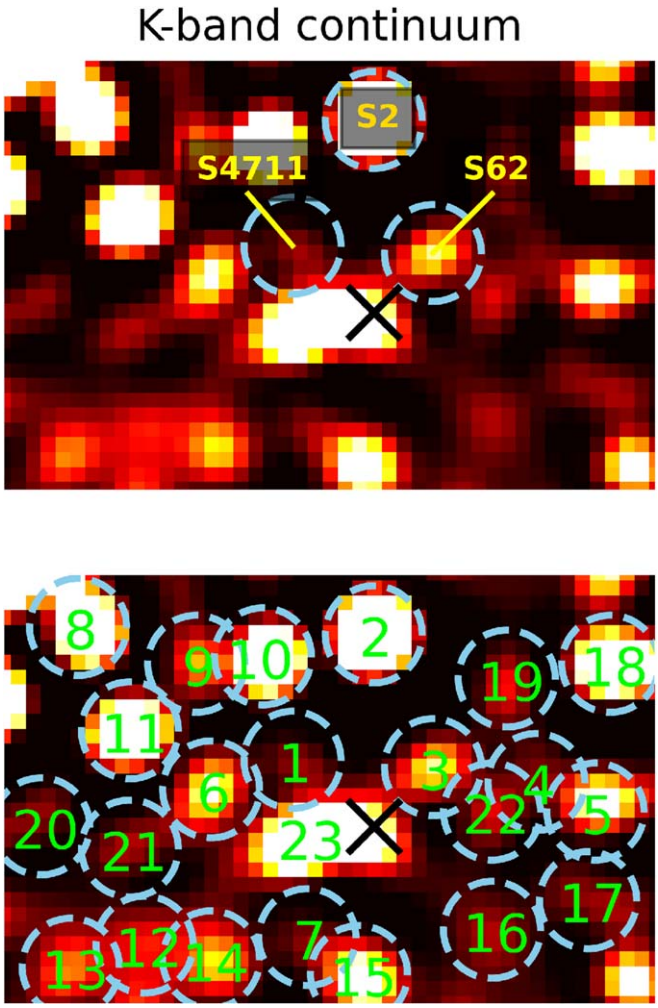

Figure 10. Finding chart for the 25 innermost objects around Sgr A* based on the NACO GC data of 2008. Both images show the same data. We mark S2, S62, and S4711 in the upper image. In the lower one, we mark all visible objects with an ID. The related objects are in consecutive order: 1/S4711, 2/S2, 3/S62, 4/S4712, 5/S38, 6/S40, 7/S4713, 8/S14, 9/S56, 10/S13, 11/S20, 12/DSO, 13/S23, 14/S54, 15/S19, 16/S4718, 17/S61, 18/S31, 19/S4714, 20/a, 21/b, 22/S4715. Next to the black x (Sgr A*), ID #23 marks the position of S17, S55, and S175. The objects 20/a and 21/b can be observed at the same position relative to Sgr A* between 2006 and 2015 and are therefore foreground or background sources.

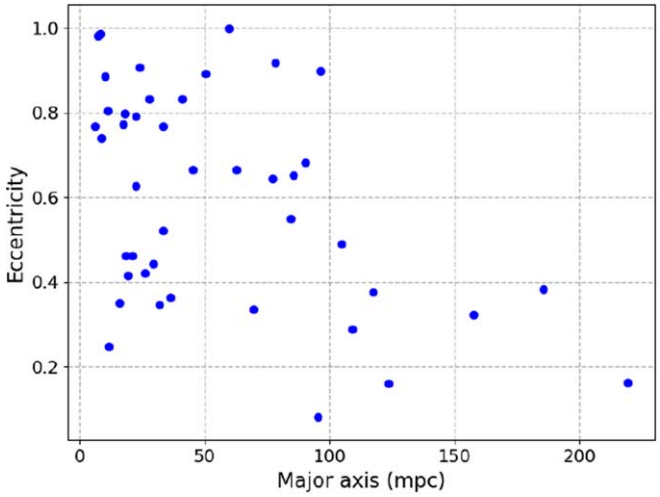

Figure 11. Eccentricity of all known S-stars as a function of the major axis. The values used the plot are based on a Keplerian fit. The related orbital elements are presented in Ali et al. (2020).

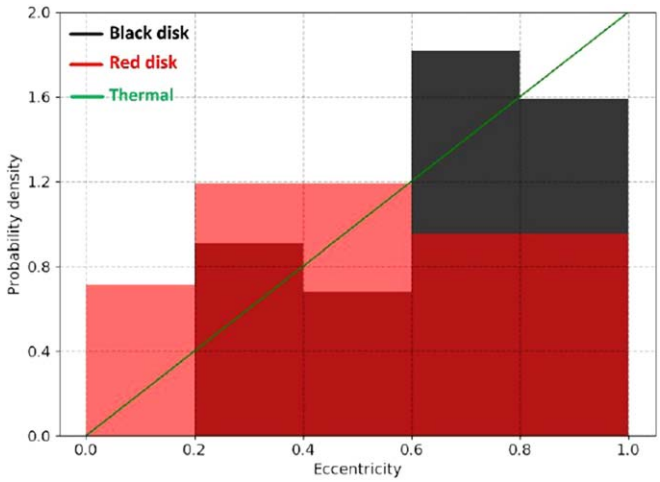

Figure 12. Distribution of eccentricities of both stellar disks identified by Ali et al. (2020) including the newly identified stars. Dark red indicates the overlap between the red and the black disk in this diagram.

blending and the overlap of other nearby stars, an observation before 2008 and after 2009 is not satisfying.

As for S4712, S4713, S4714, and S4715, it is unlikely that these stars are blended background or foreground stars. This is underlined by the observation of more than 3 consecutive years (Sabha et al. 2012; Peißker et al. 2020a). When it comes to 20/a, 21/b, and S4716, it could be argued that these stars are foreground/background stars that are passing Sgr A* at small projected distances (see Eckart et al. 2002; Ghez et al. 2002).

3.6. Eccentricity Relation

Peißker et al. (2020a), Ali et al. (2020), and this work investigate members of the S-cluster. S62, S4711, and S4714 show highly eccentric orbits with a short semimajor axis (see Table 1). In Figure 11, we show the relation between the eccentricity as a function of the major axis. We want to point out an outlier not shown in Figure 11. This outlier is S85 and is 144 mpc away from the remaining stars. This is a significant distance relative to the extent of the S-cluster of around 40 mpc. Considering the large distance from the inner arcsecond, it raises doubt about the classification of S85 as a member of the S-cluster. In light of the Hills mechanism (Hills 1988) and the work of Zajaček et al. (2014) mentioned in the introduction, a detailed analysis of S85 could be fruitful. Besides the outlier, the trend of high eccentricity followed by a low major-axis is detected for the S-stars. We find for all stars with a larger major axis (>100 mpc) eccentricity values below 0.5. And vice versa, the density distribution of S-stars with a major axis <100 mpc shows a tendency toward eccentricity values higher than 0.5.

Figure 12 shows the eccentricity distribution of known S-stars orbits, including the newly identified sources; by examining it we find that the more compact black disk (see Ali et al. 2020) exhibits a thermalized distribution ($f(e) \times de = 2e \times de$, Jeans 1919). Here, the term "thermalized" refers to reaching statistical equilibrium as a result of stellar interactions. The reason behind this may be the result of many Kozai–Lidov cycles that are triggered with the presence of a massive disturber

(Chen & Amaro-Seoane 2014; see also Ali et al. 2020). Furthermore, it cannot be excluded that the Hills mechanism could also be a contributing process, especially for $e > 0.9$. It is worth noting that the short orbital timescale of these inner stars is probably the reason why they reached the thermalized arrangement in a short time. In contrast, the red disk displays a nearly flat distribution, peaking at $e = 0.4$, i.e., not thermalized. This could be due to the longer orbital periods and the on-average larger distances from Sgr A*. Therefore, the red disk stars might still need longer time to achieve the thermalized case. Nevertheless, they could also be subject to a disk-migration process that leaves them in a non-thermalized state.

In addition to the previous possibilities, Merritt (2013b) proposed a plausible explanation for the current distribution of S-stars. Loss-cone dynamics describes the process in which the star suffers loss of angular momentum due to gravitational radiation at a very close distance to the SMBH. This leads to an orbit with high eccentricity. It is possible in this scenario that the star ends up being captured by the central mass. On the contrary, the star could evolve after some time and cross the Schwarzschild barrier, which defines the line of maximum eccentricity in the $e - a$ diagram. As soon as this is achieved, resonant relaxation (RR) is then triggered, allowing the star to gain angular momentum and thus lowering its orbital eccentricity.

Based on this argument, we conclude that the red disk may be relaxed by RR, while the black disk is subject to an angular momentum loss process. However, Ali et al. (2020) found that the timescale of the scalar resonant relaxation that changes the value of angular momentum exceeds the current estimated age of the S-stars. Regarding this fact and using Newtonian simulations, Perets et al. (2007b) show that RR could already exhibit its dynamical effects in case the nucleus has a large density of compact disturbers (e.g., a population of black holes). Therefore, along with the previously mentioned possibilities, the proposed loss-cone justification could be considered as a valid scenario that describes the current eccentricity evolution.

3.7. Kinematic Structure of the Central S-cluster

Ali et al. (2020) present a detailed analysis of the kinematics of 112 stars that are present in the high velocity S-cluster and orbit the supermassive black hole Sgr A*. They found that the distribution of inclinations and flight directions deviate significantly from a uniform distribution that one would expect in the case of random orientation of the orbits. The S-cluster stars are arranged in two almost edge-on thick disks that are located at a position angle of about $\pm 45^\circ$ with respect to the Galactic plane. With 25°, the poles of this structure are close to the LOS. The reason for this arrangement is unclear. It may be due to a resonance process that started during the formation of the cluster of young B-dwarf stars about 6 Myr ago. Another possibility is the presence of a disturber at a distance of a few arcseconds from the S-cluster.

In relation to these two disks identified by Ali et al. (2020), we find that the stars S4711, S4712, and S4713 belong to the more compact (about $<0\farcs5$ diameter) black disk, while S4714 and S4715 are members of the larger ($\sim 1''$ to $2''$ diameter) red disk. More precisely and according to the 3D visual inspection, the orbit of S4715 seems to have approximately a 30° deviation from the plane of the red disk. As for the remaining newly identified stars, their orbits fit on average to within about 10° into the two-disk scheme. This implies that even the stars currently closest (both, physically and in projection) to SgrA* follow the kinematic structure of the S-cluster.

4. Discussion and Conclusion

In this work, we derive various properties for the newly discovered faint star S4711 that we detected with SINFONI and NACO over several consecutive years. S4711 is on a 7.6 yr orbit around the SMBH Sgr A* with a high eccentricity of $e = 0.768$. With a K-band magnitude of about 18.3 it is among the fainter S-cluster members. The mean spatial orbital velocity of S4711 is about 0.5%c and is in line with other S-stars members like S62 and S2 close to Sgr A*. We can conclude that S4711 is without a doubt a member of the S-cluster. This is followed by the detection of S4712–S4715. From these stars, S4714 is the most interesting and shows comparable properties to S4711. The S-cluster star S4714 shows an even higher eccentricity than S62 of $e = 0.985$. With this, S4714 is the star with one of the highest eccentricities of the S-cluster except for S175. Given the detection of S62, S4711, and S4714 we find a population of stars on orbits smaller than that of S2. As a result of improved data analysis, we expect to find more stars of this class in the near future. The observation of S62, S4711, and S4714, as well as the increased probability of finding even closer stars on shorter orbits in the future with the Extremely Large-Telescope (~40 m diameter) underlines the prediction of Alexander & Morris (2003), who proposed the existence of the so-called squeezars. These stars are on highly eccentric orbits around a supermassive black hole and can be categorized as hot and cold squeezars (HS and CS, respectively). Additionally, Alexander & Hopman (2003) described orbital in-spiral processes. Together with Alexander & Morris (2003), the high eccentricity can be an indication of a tidal disruption event resulting in increased flare activity. The statistical behavior of Sgr A* is investigated by Witzel et al. (2012) and with this model, upcoming observations should trace footprints of a tidal disruption event. We speculate that the unusual strong IR flare observed by Do et al. (2019) could be linked to such an event.

However, additional monitoring data will help to discriminate the faint stars S4711–S4715 from the brighter cluster members in the nuclear region in which the arrangement of cluster members is changing on a weekly to yearly timescale. This could also help to confirm the relativistic periapse shift determined for S62 and S4711. Only a large coverage of the orbit can help to distinguish uncertainties from relativistic orbital parameters. Since we already observed a full orbit for S62 between 2003 and 2013, we should be able to see a relativistic footprint in the orbit of this S-star.

Furthermore, by analyzing the positional data of 20/a, 21/b (see Figure 10), and S4716 we find neither notable curvature nor significant acceleration. This is suspicious considering the short projected separation of these FSS from Sgr A*. It is more likely, that at least 20/a and 21/b are not members of the central part of the S-cluster but rather belong the the overall Galactic center stellar cluster. Because of the limited detection of S4716 for about 2 yr we speculate a blend star event, even though we detect this object in individual data sets throughout 2008 and 2009.

As discussed before, we expect several new findings of close stars/squeezars with NIR observations carried out with the ELT in the future. This assumption is based on the observation of S62, S4711, and S4714. The existence of squeezars in

combination with unusual high flaring activities of Sgr A* could be an interesting part of a scientific framework.

We thank the anonymous referee for the encouraging and positive comments. With the help of these comments, we were able to improve the paper. We thank the members of the NACO/SINFONI and ESO Paranal/Chile team. This work was supported in part by the Deutsche Forschungsgemeinschaft (DFG) via the Cologne Bonn Graduate School (BCGS), the Max Planck Society through the International Max Planck Research School (IMPRS) for Astronomy and Astrophysics, as well as special funds through the University of Cologne and SFB 956: Conditions and Impact of Star Formation. We thank the Collaborative Research Centre 956, sub-project [A02], funded by the Deutsche Forschungsgemeinschaft (DFG) project ID 184018867. M.Z. acknowledges the financial support by the National Science Centre, Poland, grant No. 2017/26/A/ST9/00756 (Maestro 9).

Facilities: VLT(SINFONI), VLT(NACO), VLT (GRAVITY).

Appendix A
Stellar Motion of S4712, S4713, S4714, and S4715

In this section, we present the orbits of S4712 (Figure A1), S4713 (Figure A2), S4714 (Figure A3), and S4715 (Figure A4). For the data points, typical uncertainties of ±6.5 mas are used. They are fully compatible with the analysis of S62 (Peißker et al. 2020a) where we use these uncertainties for the data representation in the corresponding figures. The coverage of a full orbit is not given (see Section 3). The orbital elements with the related uncertainties that are based on the MCMC simulations (Figures A5, A6, A7, A8) can be found in Table 1. For S4714, we find an orbit that is comparable to S55 when it comes to the orbital period.

Because of the crowded field of view, observing S4712, S4713, and S4715 is challenging. However, we trace these three S-cluster members in the years between 2008–2015 (S4712), 2006–2010 (S4713), and 2007–2009 (S4715). Since bright S-stars like S2, S13, S19, or S31 are contaminating the orbits of S4712, S4713, and S4715, an observation before 2006 and after 2015 is not free of confusion.

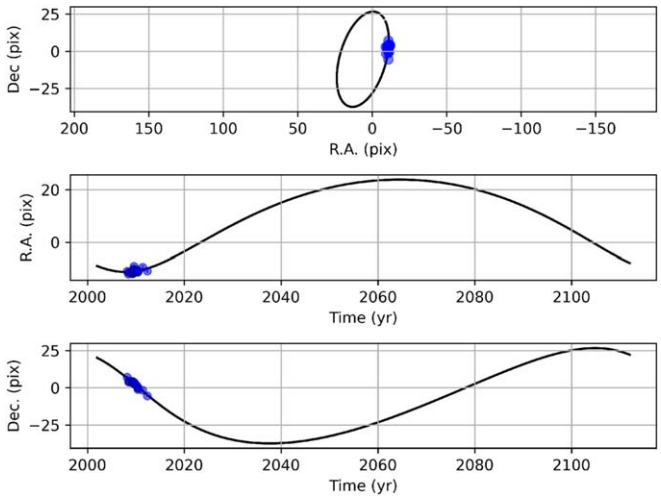

Figure A1. Detection of the stellar orbit of S4712 based on NACO data of 2008–2015. The sizes of the data points are larger than the typical spatial uncertainties of ±0.5 px. One full orbit is presented in this figure.

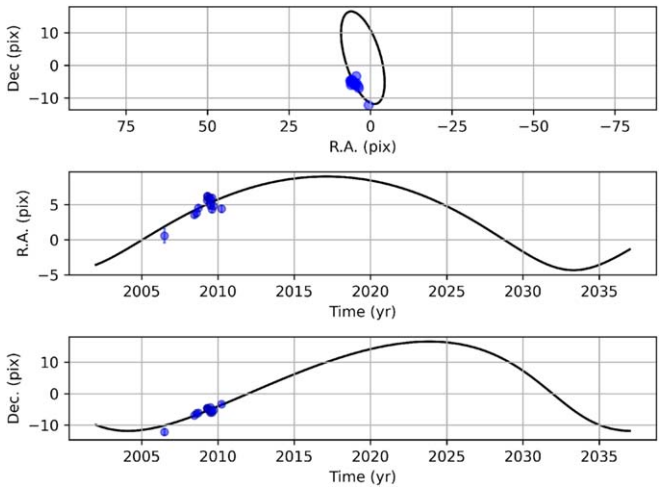

Figure A2. S4713 detected with NACO between 2006 and 2010. Except for the R.A. data point in 2006, the typical uncertainties are ±0.5 px. In 2006, the presence of the close by S-stars S17, S19, and S55 results in an increased spatial uncertainty of ±1 px.

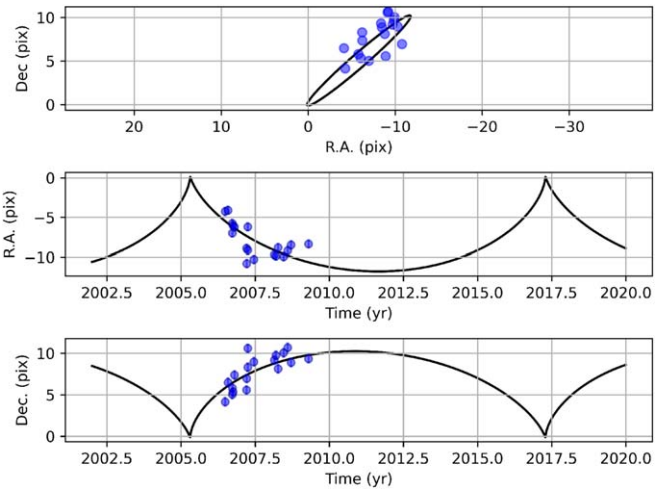

Figure A3. Detection of the stellar orbit of S4714 based on NACO data of 2006–2009. Like S55, S62, and S4711, the orbital period of S4714 is shorter compared to S2.

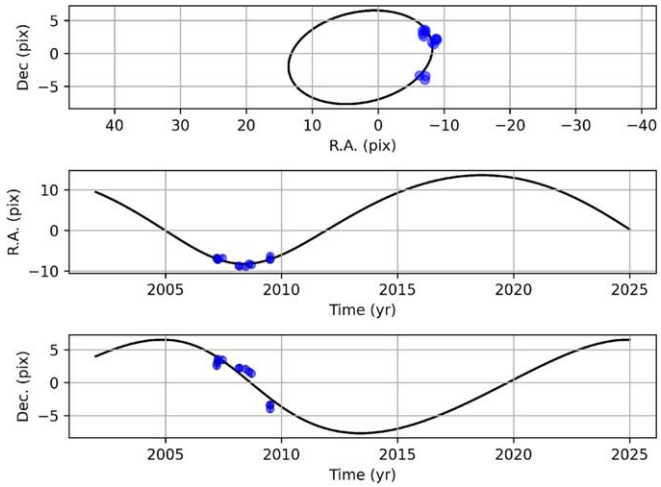

Figure A4. S4715 detected with NACO between 2007 and 2009. The uncertainties are as big as the data points and in the typical range of ±0.5 px or ±6.5 mas.

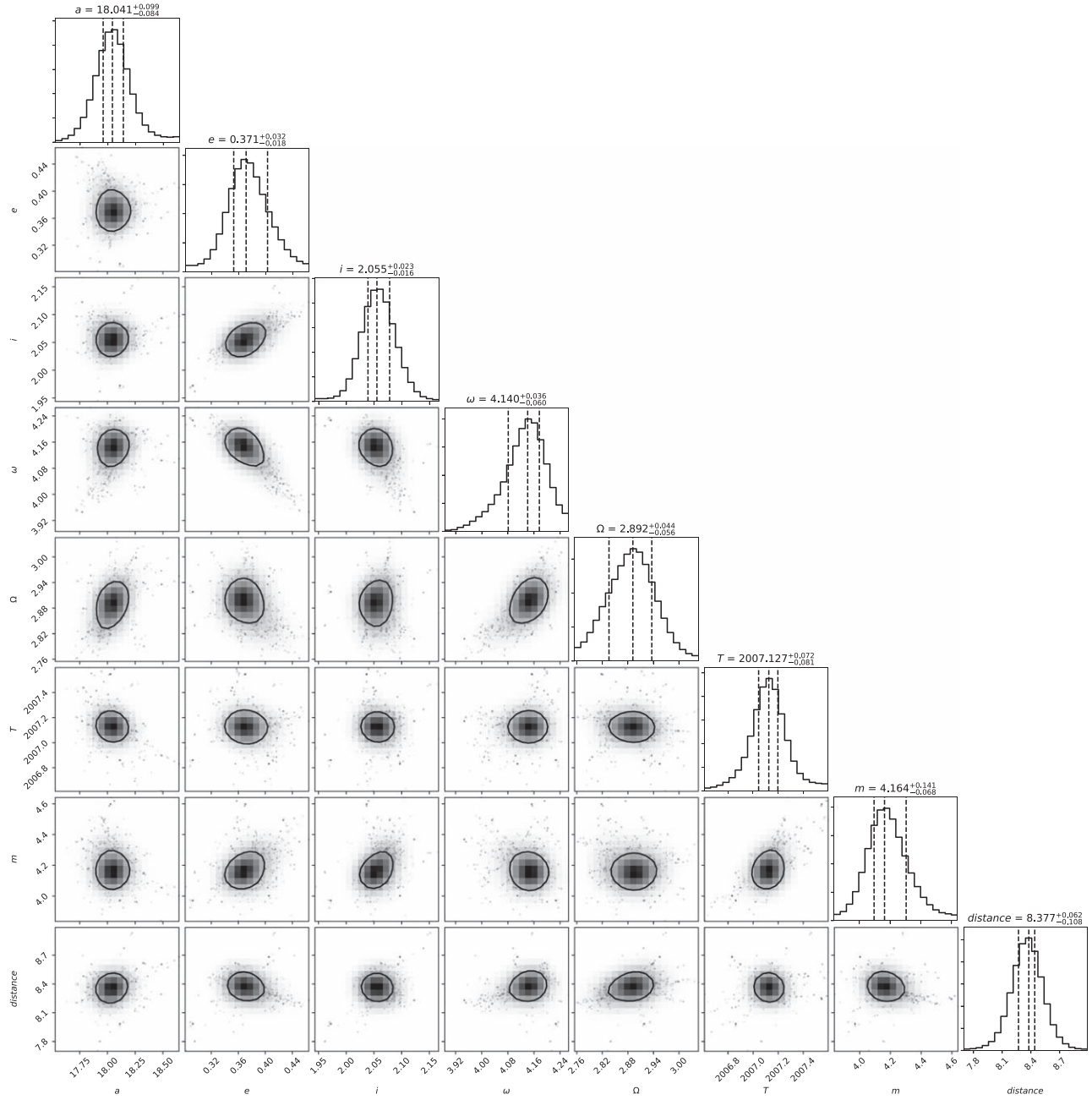

Figure A5. MCMC simulations of S4712. Like before, we additionally show the posterior distribution for the mass and distance of Sgr A*. The compact distribution of the shown parameter indicates a satisfying orbital analysis.

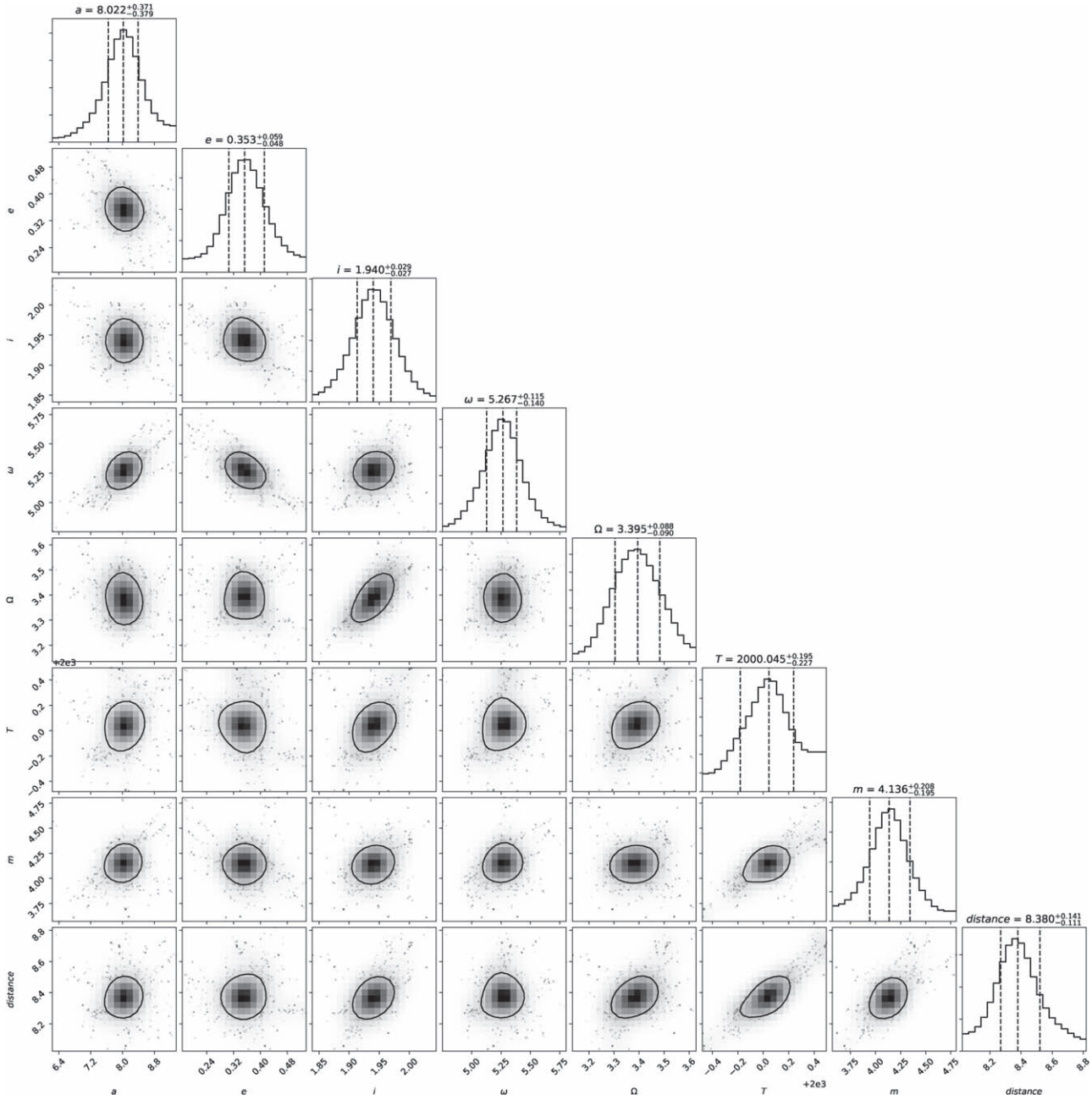

Figure A6. MCMC simulations of S4713.

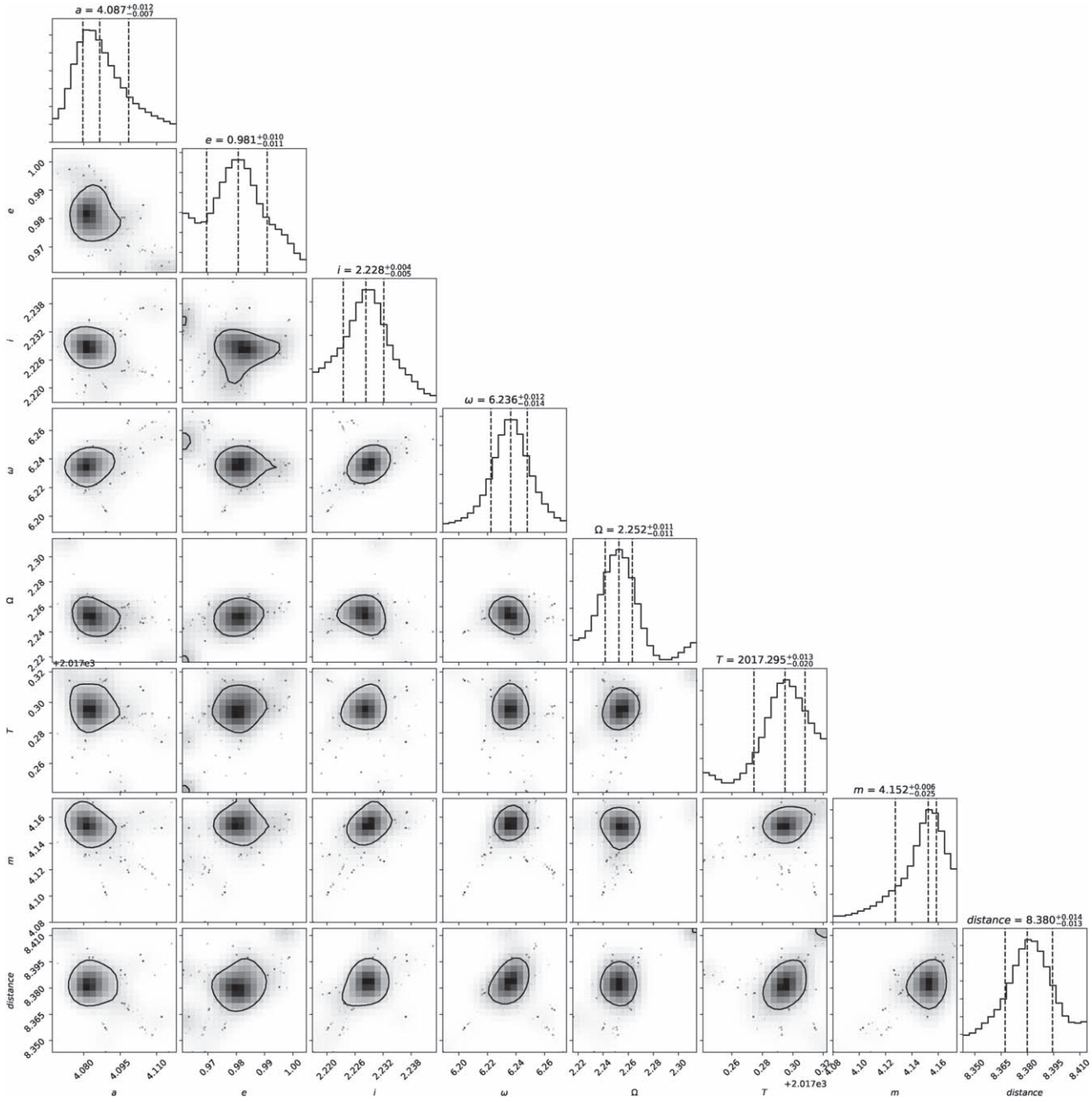

Figure A7. MCMC simulations of S4714.

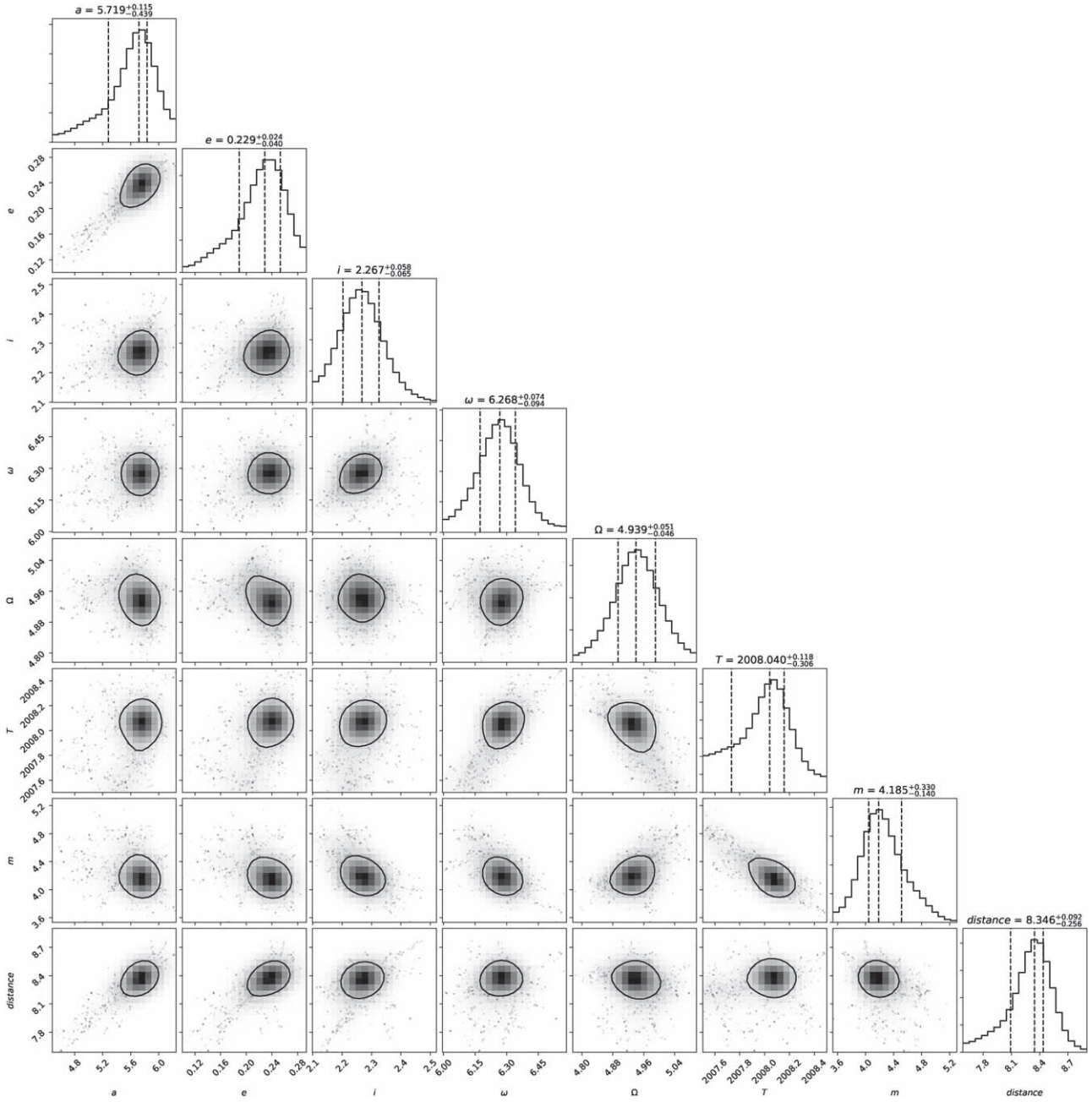

Figure A8. MCMC simulations of S4715.

Appendix B
BONNSAI Simulations of the S-star S4711

As discussed and shown in Section 3, the spectroscopic analysis of the spectrum of S4711 in combination with the photometric information provides properties that can be used for a deeper investigation. We use BONNSAI[7](Schneider et al. 2014) for that. BONNSAI is a Bayesian tool that compares properties of stars with evolution models. We use a significance level of 5% with the observables given in Table B1. The resulting parameters are included in Table B2. Like the MCMC simulations for the orbital elements of S62, S4711, …, and S4715, the probability distributions of the difference between the prior and posterior values are negligibly small (see Figure B1).

Table B1
Input Parameter of the BONNSAI Simulations

$T_{\rm eff}$ in (K)	$M_{\rm act}$ in ($M_\odot$)	$v \sin i$ in (km s^{-1})	$v_{\rm rot}$ in (km s^{-1})
11000^{+1000}_{-1000}	$2.20^{+2.0}_{-1.0}$	$239.0^{+25.0}_{-25.0}$	$263.0^{+28.0}_{-28.0}$

Note. The resulting fit parameter can be found in Table B2. The uncertainties are based the presented analysis.

[7] The BONNSAI web service is available at www.astro.uni-bonn.de/stars/bonnsai.

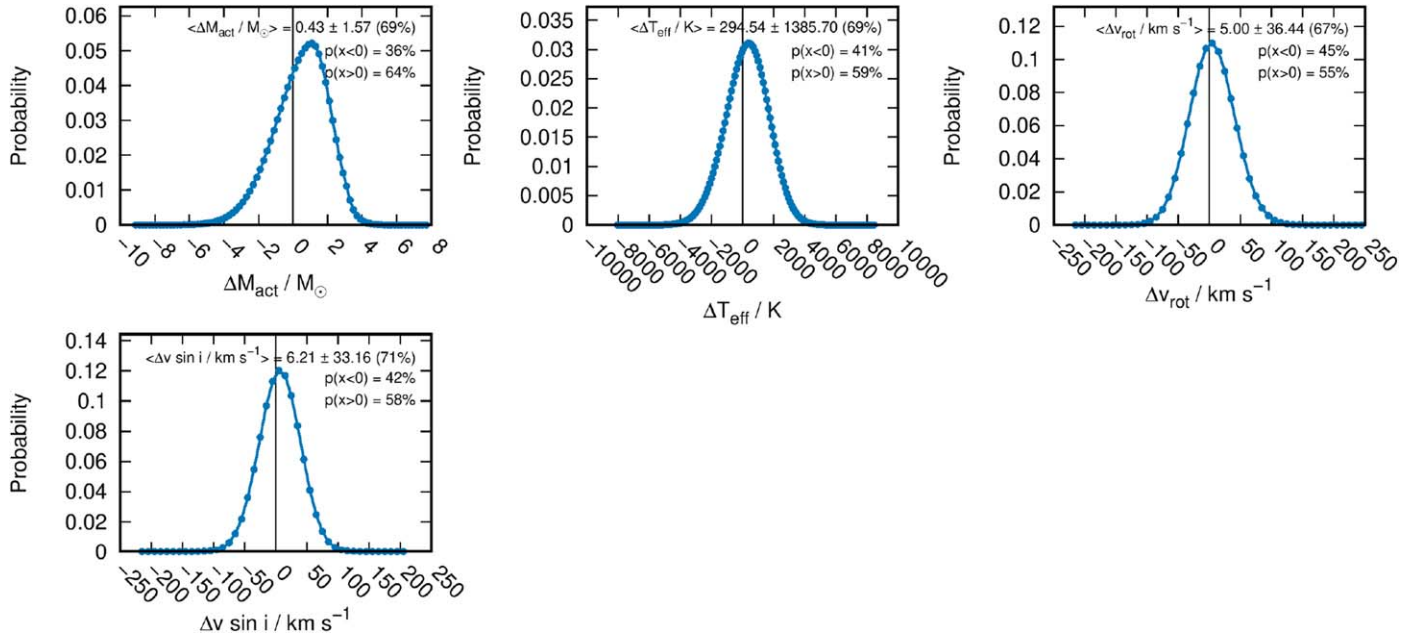

Figure B1. Difference between our prior values and the posterior values of the BONNSAI simulation.

Table B2
Output Parameter of the BONNSAI Simulations

$M_{\rm ini}$ in ($M_\odot$)	Age in (Myr)	$v_{\rm ini}$ in (km s^{-1})	$\log\frac{L}{L_\odot}$	$T_{\rm eff}$ in (K)	$M_{\rm act}$ in ($M_\odot$)	R in ($R_\odot$)	$\log\frac{g}{\rm cgs}$	$v_{\rm rot}$ in (km s^{-1})
$3.20^{+0.31}_{-0.30}$	$158.29^{+60.13}_{-56.15}$	$280.0^{+28.84}_{-32.26}$	$2.15^{+0.23}_{-0.18}$	$11587.84^{+768.39}_{-1128.75}$	$3.0^{+0.48}_{-0.10}$	$2.59^{+1.71}_{-0.55}$	$3.92^{+0.30}_{-0.28}$	$260.0^{+24.73}_{-22.58}$

Note. The uncertainties are all given at a 1σ confidence level. Considering the well-defined input parameters, the fit delivers satisfying results.

Appendix C
Data

In this section, we give an overview about the used data for the presented analysis. As mentioned in Section 2, the data were used for the studies in Parsa et al. (2017), Peißker et al. (2019, 2020a), and Peißker et al. (2020b). Partially, the data were also analyzed in Mužić et al. (2007, 2008, 2010), Witzel et al. (2012), Sabha et al. (2012), Eckart et al. (2013), Valencia-S. et al. (2015), and Shahzamanian et al. (2016). We adapt Tables C1, C2, and C3 from Peißker et al. (2020a) and Peißker et al. (2020b).

Table C1
SINFONI Data of 2007

Date (YYYY MM DD)	Observation ID	Amount of on source exposures			Exp. Time
		Total	Medium	High	(s)
2007 Mar 26	078.B-0520(A)	8	1	2	600
2007 Apr 22	179.B-0261(F)	7	2	1	600
2007 Apr 23	179.B-0261(F)	10	0	0	600
2007 Jul 22	179.B-0261(F)	3	0	2	600
2007 Jul 24	179.B-0261(Z)	7	0	7	600
2007 Sep 3	179.B-0261(K)	11	1	5	600
2007 Sep 4	179.B-0261(K)	9	0	0	600

Note. The total amount of data is listed. We also list the total amount of data. If the data cubes do not fulfill a certain quality standard (usually this can be measured by the FHWM of S2), we exclude it from the analysis.

Table C2
NACO Data between 2004 and 2009

NACO				
Date (UT)	Observation ID	Number of exposures	Total exposure time(s)	λ
2004 Jul 6	073.B-0775(A)	344	308.04	*K*
2004 Jul 8	073.B-0775(A)	285	255.82	*K*
2005 Jul 25	271.B-5019(A)	330	343.76	*K*
2005 Jul 27	075.B-0093(C)	158	291.09	*K*
2005 Jul 29	075.B-0093(C)	101	151.74	*K*
2005 Jul 30	075.B-0093(C)	187	254.07	*K*
2005 Jul 30	075.B-0093(C)	266	468.50	*K*
2005 Aug 2	075.B-0093(C)	80	155.77	*K*
2006 Aug 2	077.B-0014(D)	48	55.36	*K*
2006 Sep 23	077.B-0014(F)	48	55.15	*K*
2006 Sep 24	077.B-0014(F)	53	65.10	*K*
2006 Oct 3	077.B-0014(F)	48	53.84	*K*
2006 Oct 20	078.B-0136(A)	47	42.79	*K*
2007 Mar 4	078.B-0136(B)	48	39.86	*K*
2007 Mar 20	078.B-0136(B)	96	76.19	*K*
2007 Apr 4	179.B-0261(A)	63	49.87	*K*
2007 May 15	079.B-0018(A)	116	181.88	*K*
2008 Feb 23	179.B-0261(L)	72	86.11	*K*
2008 Mar 13	179.B-0261(L)	96	71.49	*K*
2008 Apr 8	179.B-0261(M)	96	71.98	*K*
2009 Apr 21	178.B-0261(W)	96	74.19	*K*
2009 May 3	183.B-0100(G)	144	121.73	*K*
2009 May 16	183.B-0100(G)	78	82.80	*K*
2009 Jul 3	183.B-0100(D)	80	63.71	*K*
2009 Jul 4	183.B-0100(D)	80	69.72	*K*
2009 Jul 5	183.B-0100(D)	139	110.40	*K*
2009 Jul 5	183.B-0100(D)	224	144.77	*K*
2009 Jul 6	183.B-0100(D)	56	53.81	*K*
2009 Jul 6	183.B-0100(D)	104	72.55	*K*
	183.B-0100(I)	62	48.11	*K*

Table C2
(Continued)

NACO				
Date (UT)	Observation ID	Number of exposures	Total exposure time(s)	λ
2009 Aug 10				
2009 Aug 12	183.B-0100(I)	101	77.32	*K*

Note. The total number of exposures used for the final mosaics is listed. Also, we list the added up total exposure time and the related band.

Table C3
NACO Data between 2010 and 2016

NACO				
Date (UT)	Observation ID	Number of exposures	Total exposure time(s)	λ
2010 Mar 29	183.B-0100(L)	96	74.13	*K*
2010 May 9	183.B-0100(T)	12	16.63	*K*
2010 May 9	183.B-0100(T)	24	42.13	*K*
2010 Jun 12	183.B-0100(T)	24	47.45	*K*
2010 Jun 16	183.B-0100(U)	48	97.78	*K*
2011 May 27	087.B-0017(A)	305	4575	*K*
2015 Aug 1	095.B-0003(A)	172	5160	*K*
2016 Mar 22	594.B-0498(I)	144	6300	*K*

Note. Please note that NACO was decommissioned between 2013 and 2015.

ORCID iDs

Florian Peißker https://orcid.org/0000-0002-9850-2708
Andreas Eckart https://orcid.org/0000-0001-6049-3132
Michal Zajaček https://orcid.org/0000-0001-6450-1187
Basel Ali https://orcid.org/0000-0002-5728-4054

References

Abt, H. A., Levato, H., & Grosso, M. 2002, ApJ, 573, 359
Alexander, T., & Hopman, C. 2003, ApJL, 590, L29
Alexander, T., & Morris, M. 2003, ApJL, 590, L25
Ali, B., Daria, P., Eckart, A., et al. 2020, ApJ, 896, 100
Almkvist, G., & Berndt, B. 1988, Am. Math. Mon., 95, 585
Bromley, B. C., Kenyon, S. J., Geller, M. J., & Brown, W. R. 2012, ApJL, 749, L42
Cai, R.-G., Liu, T.-B., & Wang, S.-J. 2018, arXiv:1808.03164
Chen, X., & Amaro-Seoane, P. 2014, ApJL, 786, L14
Clark, J. S., Lohr, M. E., Najarro, F., Dong, H., & Martins, F. 2018, A&A, 617, A65
Clark, J. S., & Steele, I. A. 2000, A&AS, 141, 65
Do, T., Witzel, G., Gautam, A. K., et al. 2019, ApJL, 882, L27
Eckart, A., & Genzel, R. 1996, Natur, 383, 415
Eckart, A., & Genzel, R. 1997, MNRAS, 284, 576
Eckart, A., Genzel, R., Ott, T., & Schödel, R. 2002, MNRAS, 331, 917
Eckart, A., Mužić, K., Yazici, S., et al. 2013, A&A, 551, A18
Eisenhauer, F., Genzel, R., Alexander, T., et al. 2005, ApJ, 628, 246
Foreman-Mackey, D., Hogg, D. W., Lang, D., & Goodman, J. 2013, PASP, 125, 306
Genzel, R., Eisenhauer, F., & Gillessen, S. 2010, RvMP, 82, 3121
Ghez, A. M., Duchêne, G., Matthews, K., et al. 2003, ApJL, 586, L127
Ghez, A. M., Duchene, G., Morris, M., et al. 2002, BAAS, 34, 129
Ghez, A. M., Klein, B. L., Morris, M., & Becklin, E. E. 1998, ApJ, 509, 678
Gillessen, S., Eisenhauer, F., Trippe, S., et al. 2009, ApJ, 692, 1075
Gillessen, S., Plewa, P. M., Eisenhauer, F., et al. 2017, ApJ, 837, 30

Gould, A., & Quillen, A. C. 2003, ApJ, 592, 935
Gravity Collaboration, Abuter, R., Amorim, A., et al. 2018a, A&A, 615, L15
Gravity Collaboration, Abuter, R., Amorim, A., et al. 2018b, A&A, 618, L10
Gravity Collaboration, Abuter, R., Amorim, A., et al. 2019, A&A, 625, L10
Gravity Collaboration, Abuter, R., Amorim, A., et al. 2020, A&A, 636, L5
Habibi, M., Gillessen, S., Martins, F., et al. 2017, ApJ, 847, 120
Hanson, M. M., Conti, P. S., & Rieke, M. J. 1996, ApJS, 107, 281
Hills, J. G. 1988, Natur, 331, 687
Hopman, C., & Alexander, T. 2006, ApJ, 645, 1152
Jalali, B., Pelupessy, F. I., Eckart, A., et al. 2014, MNRAS, 444, 1205
Jeans, J. H. 1919, MNRAS, 79, 408
Löckmann, U., Baumgardt, H., & Kroupa, P. 2008, ApJL, 683, L151
Lucy, L. B. 1974, AJ, 79, 745
Lumsden, S. L., Puxley, P. J., & Hoare, M. G. 2001, MNRAS, 320, 83
Merritt, D. 2013a, Dynamics and Evolution of Galactic Nuclei (Princeton, NJ: Princeton Univ. Press)
Merritt, D. 2013b, CQGra, 30, 244005
Meyer, L., Eckart, A., Schödel, R., et al. 2006, A&A, 460, 15
Meyer, L., Ghez, A. M., Schödel, R., et al. 2012, Sci, 338, 84
Mužić, K., Eckart, A., Schödel, R., et al. 2010, A&A, 521, A13
Mužić, K., Eckart, A., Schödel, R., Meyer, L., & Zensus, A. 2007, A&A, 469, 993
Mužić, K., Schödel, R., Eckart, A., Meyer, L., & Zensus, A. 2008, A&A, 482, 173
Nayakshin, S., Cuadra, J., & Springel, V. 2007, MNRAS, 379, 21
Parsa, M., Eckart, A., Shahzamanian, B., et al. 2017, ApJ, 845, 22
Peißker, F., Eckart, A., & Parsa, M. 2020a, ApJ, 889, 61
Peißker, F., Hosseini, S. E., Zajaček, M., et al. 2020b, A&A, 634, A35
Peißker, F., Zajaček, M., Eckart, A., et al. 2019, A&A, 624, A97
Perets, H. B., Hopman, C., & Alexander, T. 2007a, ApJ, 656, 709
Perets, H. B., Hopman, C., & Alexander, T. 2007b, ApJ, 656, 709
Sabha, N., Eckart, A., Merritt, D., et al. 2012, A&A, 545, A70
Schneider, F. R. N., Langer, N., de Koter, A., et al. 2014, A&A, 570, A66
Schödel, R., Najarro, F., Muzic, K., & Eckart, A. 2010, A&A, 511, A18
Shahzamanian, B., Eckart, A., Zajaček, M., et al. 2016, A&A, 593, A131
Slettebak, A., Collins, G. W. I., Boyce, P. B., White, N. M., & Parkinson, T. D. 1975, ApJS, 29, 137
Tokunaga, A. T. 2000, in Allen's Astrophysical Quantities, ed. A. N. Cox (4th ed.; New York: AIP Press), 143
Valencia-S., M., Eckart, A., Zajaček, M., et al. 2015, ApJ, 800, 125
Waisberg, I., Dexter, J., Gillessen, S., et al. 2018, MNRAS, 476, 3600
Weinberg, S. 1972, Gravitation and Cosmology: Principles and Applications of the General Theory of Relativity (Weinheim: Wiley-VCH)
Witzel, G., Eckart, A., Bremer, M., et al. 2012, ApJS, 203, 18
Zajaček, M., Karas, V., & Eckart, A. 2014, A&A, 565, A17
Zajaček, M., & Tursunov, A. A. 2018, AN, 339, 324
Zorec, J., Frémat, Y., Domiciano de Souza, A., et al. 2017, A&A, 602, A83